Check for updates

ChemSusChem

Chemistry Europe
European Chemical Societies Publishing
ChemSusChem

RESEARCH ARTICLE OPEN ACCESS

Mechanistic Insights Into Zn-Promoted CO_2 Electroreduction on α-CuZn Alloys in Aprotic Media

Niklas Oppel[1] | Liana Savintseva[2] | Philipp Röse[1] | Georg Kastlunger[3] | Felix Studt[2,4] | Ulrike Krewer[1]

[1]Institute for Applied Materials – Electrochemical Technologies, Karlsruhe Institute of Technology, Karlsruhe, Germany | [2]Institute of Catalysis Research and Technology, Karlsruhe Institute of Technology, Eggenstein-Leopoldshafen, Germany | [3]Department of Physics, Technical University of Denmark, Kongens Lyngby, Denmark | [4]Institute for Chemical Technology and Polymer Chemistry, Karlsruhe Institute of Technology, Karlsruhe, Germany

Correspondence: Ulrike Krewer (ulrike.krewer@kit.edu)

Received: 12 February 2026 | **Revised:** 28 April 2026 | **Accepted:** 1 June 2026

Keywords: bimetallic catalyst | brass | cyclic voltammetry | density functional calculations | kinetic modeling

ABSTRACT

How Zn enhances the performance of Cu electrocatalysts for CO_2RR in nonaqueous electrolytes remains an open question. Herein, we address this question by combining electrochemical measurements, kinetic modeling, and DFT calculations to elucidate Zn's role in boosting the electrocatalytic activity of Cu. Cyclic and linear sweep voltammetry reveal enhanced CO_2 reduction activity with increasing Zn content, up to threefold higher current density at 25 wt.% Zn. Kinetic modeling attributes this to improved CO_2 activation, while DFT confirms that Zn sites energetically stabilize Cu-adsorbed CO_2. This work uncovers the mechanism behind CuZn alloys' superior performance, guiding design of efficient CO_2RR catalysts for sustainable energy conversion.

1 | Introduction

Electrocatalytic CO_2 reduction (CO_2R) offers significant potential for facilitating the transition to a carbon-neutral economy by converting excess CO_2 into valuable feedstock for the chemical industry [1]. The aqueous electrolytes typically employed for CO_2R have multiple drawbacks, including limited CO_2 transport to the electrode due to low CO_2 solubility in aqueous solution [2, 3], catalyst instability leading to changes in product selectivity [4, 5], low carbon efficiency due to alkaline carbonate formation [6, 7], and the competing hydrogen evolution reaction (HER). The local reaction environment, including pH [8–10], cations [11, 12], and solvent [13, 14], has a tremendous impact on the activity of the CO_2 reduction reaction (CO_2RR).

Aprotic organic electrolytes offer higher CO_2 solubility and effectively eliminate the HER compared to aqueous electrolytes [15], yet they have received considerably less research attention [16]. The suppression of the HER allows for pure CO production without H_2 by-products, thus distinguishing aprotic CO_2R favorably from alternative CO_2R techniques. For example, CO_2R in solid oxide electrolysis cells typically comprises the HER because they cannot presently be operated without water [17]. The classical chemical CO_2 to CO pathway via the reverse water gas shift reaction requires H_2 as the reducing agent [18]. Realizing pure CO production at a commercial scale via CO_2R in aprotic organic electrolytes is thus highly attractive.

Due to the absence of protons, aprotic organic electrolytes enable distinct reaction pathways toward either CO with Faradaic efficiency (FE) beyond 95% [19] or oxalate with a FE of up to 80% [20]. One of the main drivers in deciding product selectivity is the choice of the aprotic solvent [21]. Among these, acetonitrile stands out due to its eightfold increased CO_2 solubility compared to water, a wide electrochemical stability window, and its tendency to favor CO formation over oxalate as the main product [22].

In addition to the solvent, the salt of the supporting electrolyte significantly affects CO_2R by modulating the interfacial

This is an open access article under the terms of the Creative Commons Attribution License, which permits use, distribution and reproduction in any medium, provided the original work is properly cited.

© 2026 The Author(s). *ChemSusChem* published by Wiley-VCH GmbH.

environment. Although electric double layer and cation effects have been well studied in aqueous CO_2R [23], their role in aprotic systems remains less explored. In aprotic solvents, typically quaternary alkylammonium salts with weakly coordinating anions are utilized, as alkali cations, such as Cs^+, have been shown to passivate the electrode surface [24]. Recent work has revealed a size effect of these alkylammonium cations on CO_2RR rates, attributed to changes in interfacial electric field strength: Smaller cations are closer to the electrode, thereby increasing the electric field strength and facilitating the kinetically limiting CO_2 activation [25].

Beyond modifying the local reaction environment, the structure and composition of the catalyst material are of major importance for CO_2R performance. Binary metal catalysts offer a promising approach for tuning catalytic properties by combining two elements with complementary behavior [26, 27]. Notably, the combination of earth-abundant Cu and Zn presents a compelling choice that has already been used in several electrochemical CO_2R studies over the last few years [28–30]. Additionally, the well-established use of CuZn based-catalysts in thermo-catalytic CO_2 hydrogenation to methanol underscores the potential of this catalytic system for CO_2 conversion [31, 32].

In aqueous electrolytes, Cu is known for its ability to reduce CO_2 to a broad spectrum of hydrocarbons and oxygenates with limited selectivity, while Zn primarily produces CO [33]. In combination with Cu, Zn has been reported to enhance C—C coupling rates through the transfer of adsorbed CO from Zn to neighboring Cu sites, resulting in higher CO coverages that are beneficial for C—C coupling [34, 35]. However, the precise role of Zn in CuZn catalysts remains under debate in aqueous CO_2 electrocatalysis and in thermal catalysis [36], and is even less understood in aprotic CO_2 electrolysis, for which only a single experimental study from our group has been reported to date [37].

Our previous model-assisted study of the CO_2RR over Cu in acetonitrile suggested that CO_2 adsorption on the cathode is the primary kinetic limitation, as opposed to the transport limitations of CO_2 observed in aqueous electrolytes [3, 38]. Although increasing surface roughness and elevated pressure have been shown to partially mitigate this limitation [38], the intrinsic kinetic inhibition of Cu persists. Recent experimental work on CuZn catalysts in aprotic acetonitrile has demonstrated that incorporating Zn into Cu-based catalyst nanoparticles significantly enhances the catalysts CO_2 reduction activity toward CO production [37]. This enhancement was observed exclusively for catalysts within the homogeneous α-CuZn (α-brass) alloy phase. In contrast, pure Zn and CuZn catalysts with a Zn atomic fraction of 0.5 or higher exhibited poor performance [37]. The authors proposed that Zn improves the binding of CO_2 and other oxygen-containing intermediates on the catalyst surface, thus overcoming the identified limitation of CO_2 adsorption [37]. However, the underlying mechanisms responsible for this promotional effect are not yet fully understood. Nevertheless, their elucidation is essential for the rational design of improved CO_2RR catalysts and, thus, for efficient and high-performing cells for CO_2R in organic electrolytes.

To address this knowledge gap and elucidate the role of Zn in CuZn alloys on the kinetic limitations of the CO_2RR in nonaqueous electrolytes, we conduct an in-depth multiscale kinetic investigation of the CO_2RR on Cu and CuZn alloy catalysts. We combine cyclic voltammetry (CV) with dynamic kinetic modeling to enable the microkinetic analysis of reaction rates and surface coverages. This approach provides comprehensive insight into the thermodynamic and kinetic limitations, as well as the catalyst state during operation, revealing two distinct mechanistic scenarios. Finally, we employ density functional theory (DFT) calculations to probe the atomistic origins of CO_2RR on CuZn alloys and to resolve these two mechanistic scenarios.

Dynamic kinetic modeling that reproduces experimental measurements using a set of species and charge balances is a powerful tool for unraveling complex electrocatalytic reactions [2]. It has proven effective in identifying kinetic effects, such as surface coverages [39], elucidating the interplay between CO_2RR, HER, carbonation, and transport [3], and assessing the catalyst state [40]. This methodology, further extended by Geppert et al. to binary oxide catalysts [41], can aid in understanding the role of Zn in CuZn alloys, especially when combined with DFT calculations. In our previous study, we employed dynamic kinetic modeling to identify CO_2 adsorption as the rate-limiting step of the CO_2RR on Cu in acetonitrile [38]. However, the experimentally observed performance improvements of binary catalysts, such as CuZn, have not yet been systematically analyzed or mechanistically understood.

Atomistic simulations, particularly those based on DFT, are crucial to gain mechanistic insights into electrochemical reactions at electrode surfaces, such as the CO_2RR [42, 43]. The widely used computational hydrogen electrode approach excels in aqueous systems but fails to capture kinetics or apply to aprotic solvents due to its reliance on proton activity in water [44–47]. To address this, we employ DFT calculations within the so-called sawtooth potential framework as the simplest model of an electrochemical interface [48], followed by analysis using grand canonical DFT (GC-DFT), implemented through a constant charge methodology with an implicit solvation model [49]. This approach was extended by the recently proposed computational ferrocene electrode (CFE) model [50, 51], which enables a direct connection between the electrochemical potential and the electrode potential on the experimental scale. Combined with dynamic kinetic modeling, our DFT calculations yield adsorption energetics for CO_2 and CO, as well as CO_2 activation onset potentials on Cu and CuZn surfaces. Crucially, we demonstrate for the first time that the CFE approach provides a physically meaningful reference for electrocatalytic processes in aprotic media, thereby resolving ambiguous kinetic scenarios and enabling a more accurate investigation of the CO_2RR mechanism.

This work presents the first in-depth model-assisted analysis of the CO_2RR kinetics in aprotic electrolyte on CuZn alloys in the α-phase to reveal the intrinsic performance-enhancing role of Zn in the binary alloy. First, we present the experimental performance of α-CuZn electrocatalysts for CO_2R in aprotic electrolyte, followed by an in-depth analysis using our dynamic kinetic model to elucidate the influence of the Zn content on the rates and surface coverages of intermediates. DFT calculations complement the experimental and modeling results by exploring CO_2 and CO adsorbate properties and electron transfer energetics on Cu and Zn sites of the alloys. This approach yields a

1864564x, 2026, 21, Downloaded from https://chemistry-europe.onlinelibrary.wiley.com/doi/10.1002/cssc.70800 by Karlsruher Institut Fur Technologie, Wiley Online Library on [10/11/2026]. See the Terms and Conditions (https://onlinelibrary.wiley.com/terms-and-conditions) on Wiley Online Library for rules of use; OA articles are governed by the applicable Creative Commons License

holistic, quantitative understanding of Zn's role on the kinetic limitations during CO_2RR.

2 | Results and Discussion

This study investigates the CO_2 reduction on α-CuZn alloy electrocatalysts with 10%, 20% and 25% Zn mass fractions, denoted as CuZn10, CuZn20, and CuZn25, respectively. These correspond to approximate atomic compositions of Cu_9Zn, Cu_4Zn, and Cu_3Zn. The electrochemical performance of pure Cu and Zn serves as benchmark. X-ray diffraction patterns confirm a single-phase, face-centered cubic crystal structure for all α-CuZn alloy samples (Figure S1). The structural stability of the α-brass phase under these specific aprotic reaction conditions is confirmed by our recent operando X-ray absorption spectroscopy study on CuZn nanoparticles [37], which showed no significant changes in the bulk oxidation state or local coordination during cathodic polarization. However, as this technique does not resolve the surface layer, reaction-induced changes in surface roughness or near-surface Zn redistribution of the planar electrodes used in this work cannot be entirely excluded.

2.1 | Experimental Performance of α-CuZn Electrocatalysts

The electrochemical behavior of planar Cu, Zn, and α-CuZn alloys was investigated via CV and LSV in cathodic direction from −0.8 to −2.4 V in CO_2-saturated 0.1 mol L^{-1} $TBABF_4$ in acetonitrile electrolyte at room temperature (Figure 1, see Experimental Section for details). All potentials in this work are referenced to Ag/AgCl (KCl_{sat} in H_2O).

Figure 1a shows an increase in the maximum current density with an increase in Zn content for CVs at 200 mV s^{-1}. In contrast, pure Zn exhibits the lowest current density and a delayed onset potential of −2.0 V compared to Cu and the CuZn alloys. A similar trend is observed at slower scan rates, e.g., 50 mV s^{-1} (Figure 1b), although the order of CuZn10 and CuZn20 is reversed. In the LSV measurements at 1 mV s^{-1} (Figure 1c), the trend of increasing current density with increasing Zn content in the CuZn alloys is preserved. Although pure Zn reaches a slightly higher current density at the most negative potential, it again shows a significantly delayed onset.

Contrary to previous reports on CuZn nanoparticle catalysts [37], we did not observe an optimum in CO_2 reduction activity at CuZn20. Instead, CuZn25 consistently demonstrates the highest CO_2R performance under all tested conditions.

The CVs for Cu and the α-CuZn alloys exhibit a noticeable hysteresis that increases with a lower scan rate. As demonstrated in our previous work on Cu, this occurs because slower scan rates allow the system to spend more time at highly cathodic potentials, leading to a larger hysteresis width in the surface coverages of adsorbed intermediates [38]. In contrast, the CV of pure Zn shows minimal hysteresis.

The onset potential in the CVs, shown in the inset of Figure 1b, shifts to less negative values with increasing Zn content, indicating improved catalytic activity. This trend is also consistent with observations reported in the literature for Zn-rich α-CuZn nanoparticles [37]. The Tafel plots of Cu and α-CuZn alloys (inset of Figure 1c) exhibit complex behaviors with several changes in slope as a function of potential. However, three regions of approximately linear behavior can be roughly identified: (i) an initial high-slope region before the onset of electrochemical reactions, (ii) followed by a flatter intermediate region, and finally, (iii) another region of high slope at potentials below −1.7 V. This multi-regime response violates the underlying assumptions of classical Tafel analysis, which presumes a single dominating rate-determining step and constant coverage [52]. Consequently, a direct extraction of the charge transfer coefficient (α) from the experimental Tafel slopes is not feasible as the slopes do not represent a single elementary event [52, 53]. Therefore, dynamic microkinetic modeling is employed as a more robust technique to resolve changing surface coverages, identify potential-dependent rate-determining steps, and disentangle adsorption equilibria from transient rate profiles [2, 39, 40]. This approach

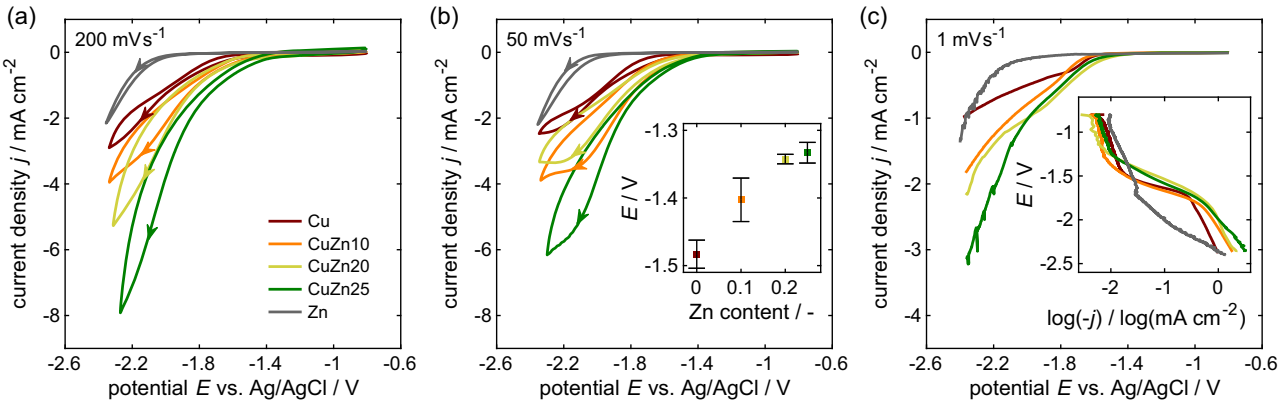


FIGURE 1 | Electrochemical characterization of Cu, Zn, and α-CuZn electrocatalysts in stagnant CO_2-saturated 0.1 mol L^{-1} $TBABF_4$ acetonitrile electrolyte: (a) Cyclic voltammograms (CVs) obtained at 200 mV s^{-1}, (b) CVs obtained at 50 mV s^{-1} with inset showing the onset potential as a function of Zn content, (c) LSV curves obtained at 1 mV s^{-1} with inset showing the corresponding Tafel plot. The CVs represent the averages of the third cycle from three independent measurements. For the full experimental dataset, see Figures S4–S9. Potentials are *iR*-corrected and referenced against Ag/AgCl (KCl_{sat} in H_2O). Arrows indicate sweep direction.

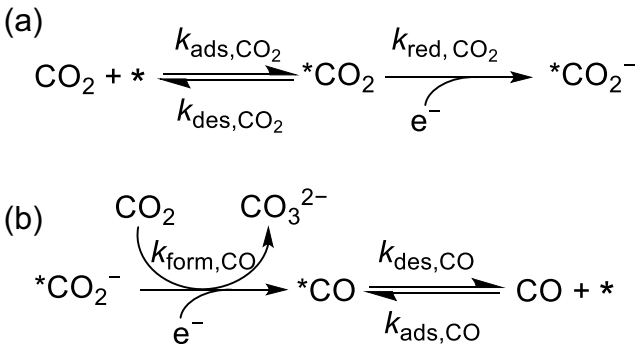
1864564x, 2026, 21, Downloaded from https://chemistry-europe.onlinelibrary.wiley.com/doi/10.1002/cssc.70800 by Karlsruher Institut Fur Technologie, Wiley Online Library on [10/11/2026]. See the Terms and Conditions (https://onlinelibrary.wiley.com/terms-and-conditions) on Wiley Online Library for rules of use; OA articles are governed by the applicable Creative Commons License

allows for a determination of kinetic parameters, such as α, by accounting for the dynamic potential-dependent behavior rather than relying on steady-state treatments [3, 38].

For Cu and α-CuZn alloys, the absolute values of the current densities decrease with decreasing scan rate in the CVs, indicating a transport or adsorption limitation. Investigating these limitations across the CuZn alloy series may reveal the specific contribution of Zn to enhanced catalytic performance. Therefore, in the following section, we apply a one-dimensional dynamic kinetic model of the cathodic half-cell to explore these limitations with the aim of identifying the origin of the enhanced performance of the CuZn alloys.

2.2 | Kinetic Model-Assisted Analysis

The physicochemical model and simulation framework employed in this study are based on our previous work [38] and are detailed in the Computational Methods section. The model describes the electrochemical reaction kinetics, the adsorption–desorption of CO_2 and CO on the surface, and one-dimensional diffusion of CO_2, CO, and CO_3^{2-} within the Nernst diffusion layer of a cathodic half-cell with a planar electrode in stagnant, CO_2-saturated acetonitrile/$TBABF_4$ electrolyte during a CV. Identifying limiting steps using steady-state methods, such as polarization curves, is challenging because all rates are constrained to be equal. Therefore, we analyze these quantities under dynamic conditions to gain crucial insight into the prevailing limiting processes and to understand how Zn alloying influences them in the α-CuZn alloys.



SCHEME 1 | Reaction mechanism for CO_2 reduction on Cu and α-CuZn electrodes in dry aprotic electrolytes, as implemented in the kinetic model, and corresponding reaction and sorption rate constants k_i: (a) CO_2 activation, and (b) CO formation and desorption.

The assumed reaction mechanism involves reversible CO_2 adsorption, one-electron reduction to $*CO_2^-$ (where * denotes the adsorbed species), electrochemical disproportionation with nearby CO_2 to form *CO and CO_3^{2-}, and CO desorption (Scheme 1). In line with the negligible CO_2RR activity of pure Zn and the Cu-like shape of the alloy CVs, the kinetic model treats only Cu-type sites as explicitly active, while the effect of Zn is captured indirectly through the fitted kinetic parameters.

Double-layer capacitances were determined from CV scan-rate dependence, electrolyte resistances were obtained from electrochemical impedance spectroscopy (EIS), and transport and solubility parameters were estimated using empirical correlations (see Table 1). The kinetic parameters were determined for each alloy composition separately by reproducing the experimental CVs at different scan rates. For pure Cu, two distinct sets of kinetic parameters were identified (Table 2), both of which reproduce the experimental CV data well for Cu, with similar normalized root mean squared errors of 0.0354 and 0.0350 (Table S7). The simulations with the corresponding parameters are labeled as Case A and Case B, respectively, and are shown in Figures 2a and 3a. As shown in Figure 4, both sets of parameters warrant further analysis as they exhibit significantly different parameters that lead to distinct conclusions about the underlying limitations.

TABLE 1 | Model parameters used in the kinetic simulations of CO_2 reduction on Cu-based catalysts in 0.1 mol L^{-1} $TBABF_4$ in acetonitrile.

Parameter	Symbol	Value	Unit
Geometric surface area of electrode	A	1.9635×10^{-5}	m^2
Areal double-layer capacitance of Cu electrode[a]	$C_{dl,Cu}$	0.124	mF cm^{-2}
Areal double-layer capacitance of CuZn10 electrode[a]	$C_{dl,CuZn10}$	0.050	mF cm^{-2}
Areal double-layer capacitance of CuZn20 electrode[a]	$C_{dl,CuZn20}$	0.031	mF cm^{-2}
Areal double-layer capacitance of CuZn25 electrode[a]	$C_{dl,CuZn25}$	0.027	mF cm^{-2}
Uncompensated internal resistance[b]	R_u	86	Ω
Initial CO_2 concentration ($p = 1013.25$ hPa, $T = 298$ K)[c]	$c_{CO_2,0}$	0.278	mol L^{-1}
Henry solubility coefficient of CO_2 in acetonitrile[c]	H_{CO_2}	0.3113	mol L^{-1} bar^{-1}
Binary liquid diffusion coefficient of CO_2 in acetonitrile[d]	D_{CO_2}	4.617×10^{-9}	m^2 s^{-1}
Binary liquid diffusion coefficient of CO in acetonitrile[d]	D_{CO}	5.043×10^{-9}	m^2 s^{-1}
Binary liquid diffusion coefficient of CO_3^{2-} in acetonitrile[e]	$D_{CO_3^{2-}}$	4.352×10^{-9}	m^2 s^{-1}

[a]From CV measurement (Figure S10).
[b]From EIS measurement (cf. section Electrochemical measurements).
[c]Calculated from Ref. [54].
[d]Calculated from Ref. [55].
[e]Estimated by linear extrapolation of the diffusion coefficients of CO_2 and CO, based on their respective molecular weight.

1864564x, 2026, 21, Downloaded from https://chemistry-europe.onlinelibrary.wiley.com/doi/10.1002/cssc.70800 by Karlsruher Institut Fur Technologie, Wiley Online Library on [10/11/2026]. See the Terms and Conditions (https://onlinelibrary.wiley.com/terms-and-conditions) on Wiley Online Library for rules of use; OA articles are governed by the applicable Creative Commons License

TABLE 2 | Kinetic parameters k_j, charge transfer coefficients α_i, and areal concentration of adsorption sites Γ for Cases A and B identified from the analysis of CV data. A graphical overview of the identified parameters is shown in Figure S20.

		α_{red,CO_2}	$\alpha_{form,CO}$	Γ	k_{ads,CO_2}	k_{des,CO_2}	k_{red,CO_2}	$k_{form,CO}$	$k_{des,CO}$	$k_{ads,CO}$
		–	–	mol m^{-2}	mol s^{-1} m^{-2}	mol s^{-1} m^{-2}	mol s^{-1} m^{-2}	mol s^{-1} m^{-2}	mol s^{-1} m^{-2}	mol s^{-1} m^{-2}
Case A	Cu	0.8261	0.9144	1.834×10^{-3}	5.424×10^{-4}	4.314×10^{-3}	4.208×10^{-9}	1.229×10^{-5}	2.300	1.027×10^{-5}
	CuZn10	0.8261	0.8571	2.208×10^{-3}	7.542×10^{-4}	6.182×10^{-3}	9.096×10^{-9}	4.455×10^{-8}	3.813	2.108×10^{-6}
	CuZn20	0.8264	0.8609	2.017×10^{-3}	1.220×10^{-3}	9.980×10^{-3}	1.837×10^{-8}	3.382×10^{-8}	3.696×0^{-4}	6.757×10^{-13}
	CuZn25	0.8264	0.8532	4.352×10^{-3}	1.273×10^{-3}	6.658×10^{-3}	1.948×10^{-8}	4.016×10^{-8}	8.278	1.451×10^{-6}
Case B	Cu	0.8470	0.7752	1.249×10^{-4}	7.785×10^{-2}	8.817×10^{-3}	1.262×10^{-9}	1.005×10^{-10}	1.425×10^{-4}	1.018×10^{-9}
	CuZn10	0.8158	0.7971	1.646×10^{-4}	9.924×10^{-2}	9.475×10^{-10}	1.251×10^{-10}	1.458×10^{-10}	2.081×10^{-4}	3.219×10^{-18}
	CuZn20	0.8158	0.6721	3.278×10^{-4}	1.741×10^{-2}	9.474×10^{-3}	2.587×10^{-10}	1.700×10^{-10}	1.891×10^{-4}	3.219×10^{-7}
	CuZn25	0.8173	0.6096	4.293×10^{-4}	9.531×10^{-2}	5.328×10^{-3}	2.587×10^{-10}	7.170×10^{-8}	3.495×10^{-4}	3.459×10^{-20}

Case A aligns with our earlier work on Cu and features comparatively slow CO_2 adsorption but fast CO formation and desorption. Its CV simulations predict that CO_2 adsorption and the first electron transfer are rate limiting, while CO coverage remains negligible (Figure 5). Therefore, activity at highly cathodic potentials is mainly constrained by CO_2 activation.

In contrast, Case B exhibits a CO_2 adsorption rate constant that is about a hundred times higher, but a substantially smaller CO desorption rate constant, i.e., k_{ads,CO_2} is about two orders of magnitude larger, while $k_{des,CO}$ is roughly 1×10^4 times smaller than in Case A (Figure 4). With these parameters, the model predicts extensive CO accumulation (>80% coverage) and a strong decline in available free sites at cathodic potentials (Figure 6). Thus, product removal, i.e., CO desorption, becomes the dominant limitation, effectively imposing CO poisoning on the Cu surface in Case B.

Since CuZn catalysts outperform pure Cu, the alloys must at least partially overcome these identified limitations. The next step is, therefore, to examine whether the Cu parameter sets can be transferred to the CuZn alloys with only modest adjustments, and which parameters, and thus kinetic process steps, are primarily responsible for the kinetic change. If reproducing the data requires larger changes in the parameters, this Case is regarded less mechanistically likely. To test whether the changes in performance with Zn content could be captured by improving a single elementary step, individual kinetic parameters were varied, and the resulting CVs were compared to those of the CuZn alloys (Figures S22 and S23). The analyzed behavior comprises simultaneous increases in current density, shift of the onset potential, and nearly unchanged hysteresis with increasing Zn content. As no single parameter reproduces the experimentally observed effect of Zn content, this indicates the need for multiparameter optimization. Consequently, for each Case (A and B), separate multiparameter optimizations were carried out to obtain composition-specific kinetic parameter sets for every CuZn alloy (Table 2).

Exemplarily shown for 50 and 200 mV s^{-1} in Figure 2, the model underlying Case A reproduces the experimental data across all compositions and scan rates, including the observed trends of increasing current density with increasing Zn content and increasing scan rate, as well as changes in the characteristic hysteresis. The same holds for additional scan rates in Figures S16–S19. The largest deviations between simulated and experimental data are observed for CuZn10. This is linked to the larger experimental variability observed for both CuZn10 and CuZn25 in three independent measurements (Figures S5 and S7). These two compositions exhibited significantly higher and nearly identical mean relative standard deviations of 0.155 and 0.144, respectively, compared to Cu (0.060) and CuZn20 (0.080). The precise origin of this variance remains unclear but is likely multifactorial, potentially stemming from sensitivities during mechanical polishing combined with distinct initial crystallographic orientations (Figure S1). Notably, while CuZn25 exhibits a similarly large experimental spread to CuZn10, it is reproduced much more accurately by the model, yielding the lowest normalized root mean squared error (Table S7). This apparent discrepancy is resolved by examining the nature of the experimental scatter: The CuZn25 replicates differ mostly in overall

1864564x, 2026, 21, Downloaded from https://chemistry-europe.onlinelibrary.wiley.com/doi/10.1002/cssc.70800 by Karlsruher Institut Fur Technologie, Wiley Online Library on [10/11/2026]. See the Terms and Conditions (https://onlinelibrary.wiley.com/terms-and-conditions) on Wiley Online Library for rules of use; OA articles are governed by the applicable Creative Commons License

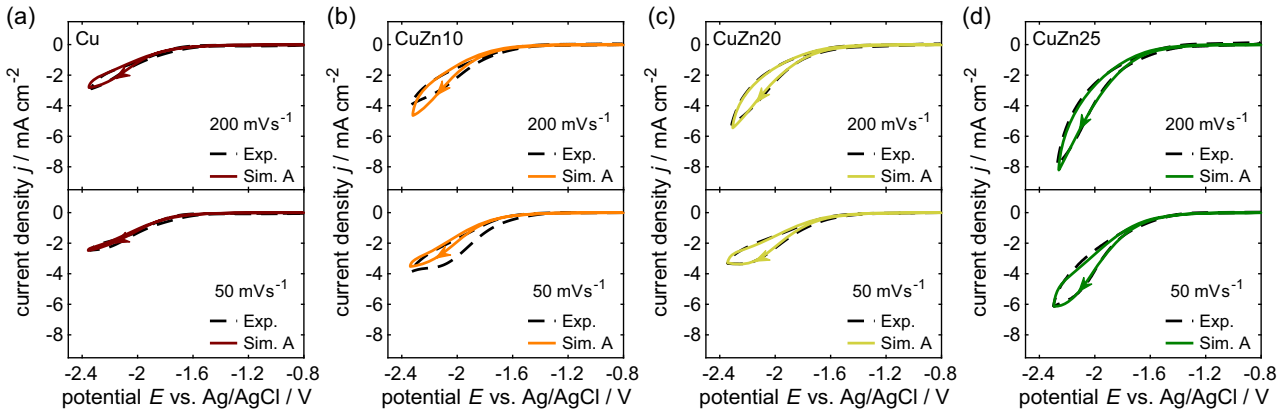


FIGURE 2 | Experimental (dashed, black) and simulated (solid, colored) CVs for CO_2 reduction on (a) Cu, (b) CuZn10, (c) CuZn20, and (d) CuZn25 electrocatalysts obtained at 200 and 50 mV s^{-1} in CO_2-saturated 0.1 mol L^{-1} $TBABF_4$ in acetonitrile electrolyte at room temperature. Simulated curves are based on the kinetic parameter sets of Case A.

magnitude, preserving the fundamental CV shape, which the kinetic model captures effectively. In contrast, the variance for CuZn10 includes small but critical variations in the CV shape and characteristic hysteresis. Because the optimization objective function is highly sensitive to transient shape features, this structural variance results in the larger model deviations observed for CuZn10.

Figure 3 reveals for 50 and 200 mV s^{-1} that the model underlying Case B also captures qualitative trends but fails to reproduce the magnitude of hysteresis consistently (for further scan rates, see Figures S16–S19). For CuZn10 and CuZn25 at low scan rates, hysteresis is underestimated; for CuZn20 at high scan rates, it is overestimated. Further optimization of Case B's parameters did not yield significant improvements, suggesting that it may represent a local minimum that does not fully reflect the complex interplay of factors influencing the electrocatalytic activity of α-CuZn alloys.

The identified parameters for Cases A and B exhibit mostly smooth trends with increasing Zn content within each Case, with only minor outliers (Table 2). However, the absolute parameter values differ markedly between Case A and Case B, with some dependencies on Zn content aligning while others oppose each other, yielding contrasting interpretations of Zn's promotional role in CO_2R. Outliers are attributed to inherent uncertainties in parameter estimation—a common challenge in kinetic modeling arising from parameter identifiability issues, model simplifications, and experimental variability [56, 57]. This was particularly evident for the CO desorption and adsorption rate constants of CuZn20 in Case A (Figures 4 and S20). Adjusting these parameters to follow a linear trend with the other alloys (as shown in Figures S24 and S25) yielded slightly poorer CV fits but restored consistency with the behavior across the series. Thus, the analysis emphasizes overall trends across the alloy series rather than individual compositions.

In Case A, the rate constant for CO_2 adsorption (k_{ads,CO_2}) increases slightly with Zn content; however, due to a similar trend in the CO_2 desorption rate constant, the equilibrium constant K_{ads,CO_2} does not change with increasing Zn content (Figure S20). Thus, Case A suggests a negligible influence of the Zn content on the net CO_2 adsorption rate. However, the CO_2 reduction rate constant (k_{red,CO_2}) increases with increasing Zn content as well (Figure 4c), suggesting that improved CO_2 activation plays a significant role in Case A.

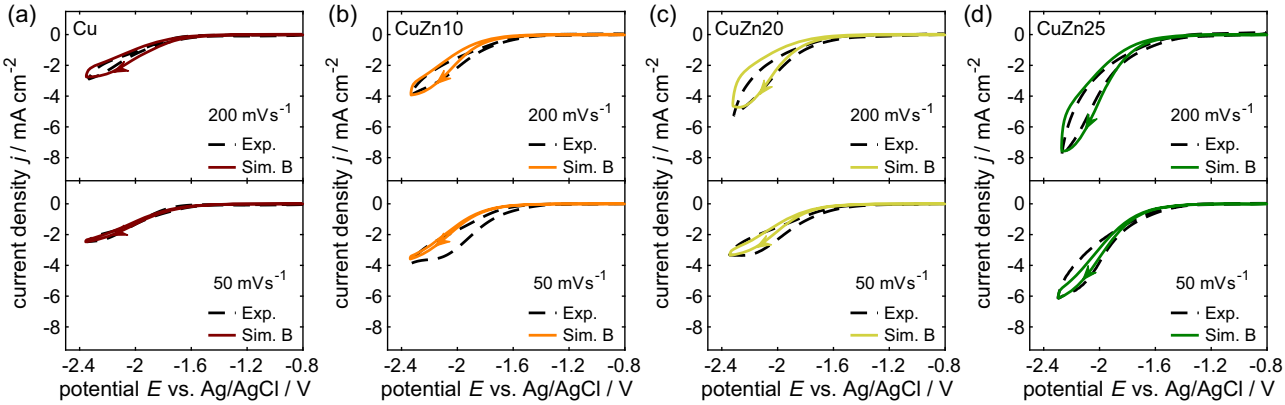


FIGURE 3 | Experimental (dashed, black) and simulated (solid, colored) CVs for CO_2 reduction on (a) Cu, (b) CuZn10, (c) CuZn20, and (d) CuZn25 electrocatalysts obtained at 200 and 50 mV s^{-1} in CO_2-saturated 0.1 mol L^{-1} $TBABF_4$ in acetonitrile electrolyte at room temperature. Simulated curves are based on kinetic parameter sets of Case B.

1864564x, 2026, 21, Downloaded from https://chemistry-europe.onlinelibrary.wiley.com/doi/10.1002/cssc.70800 by Karlsruher Institut Fur Technologie, Wiley Online Library on [10/11/2026]. See the Terms and Conditions (https://onlinelibrary.wiley.com/terms-and-conditions) on Wiley Online Library for rules of use; OA articles are governed by the applicable Creative Commons License

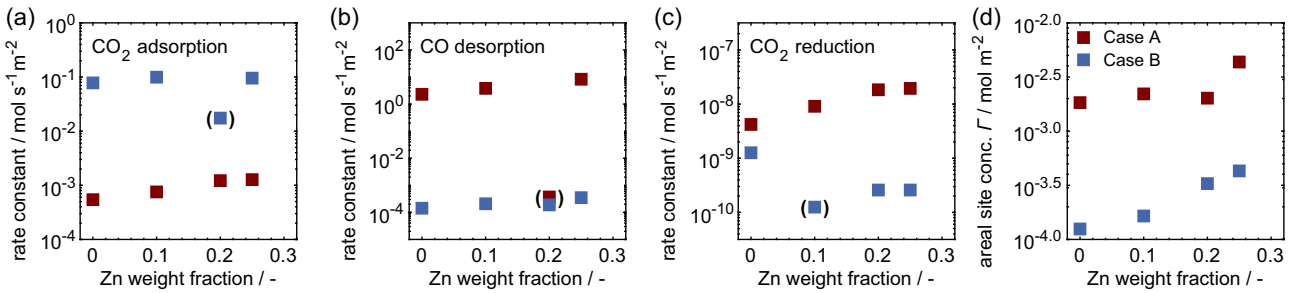


FIGURE 4 | Selection of the identified parameter values for Case A (red) and B (blue) as a function of Zn weight fraction. Cases A and B refer to distinct kinetic parameter sets obtained from model optimization against CV data for CuZn alloys, representing alternative mechanistic explanations for enhanced CO_2 reduction activity with Zn alloying. (a) CO_2 adsorption rate constant k_{red,CO_2}, (b) CO formation rate constant $k_{form,CO}$, (c) CO desorption rate constant $k_{des,CO}$ and (d) areal concentration of adsorption sites Γ. The complete parameter sets are shown in Table 2 and Figure S20. Outliers are marked by brackets ( ).

In contrast, in Case B, the rate constant for CO_2 reduction (k_{red,CO_2}) decreases with Zn content, while the rate constants for CO formation ($k_{form,CO}$) and CO desorption ($k_{des,CO}$), including the equilibrium constant (Figure S20), show a slight increase. In this Case, therefore, Zn would improve performance via faster CO formation and desorption. This difference is also reflected in the sensitivity plots: Unlike Case A, where the simulated CV current is most sensitive to changes in the CO_2 adsorption rate constant (Figure S22), the model output for Case B is most sensitive to an increase in the CO desorption rate constant (Figure S23).

Furthermore, both Cases predict a higher areal concentration of adsorption sites (Γ) for the CuZn25 alloy compared to pure Cu (Figure 4), namely a 2.4-fold increase for Case A and a 3.4-fold increase for Case B. In Case B, Γ increases systematically with Zn content, whereas in Case A, the apparent increase is largely driven by single data point (CuZn25), whereas CuZn10 and CuZn20 have similar values compared to Cu, such that a nearly constant Γ throughout the series cannot be excluded if CuZn25 is an outlier. The trend of increasing Γ with Zn content appears counterintuitive when compared to the experimental double-layer capacitance measurements (Table 1), which show a decreasing trend in the order Cu > CuZn10 > CuZn20 > CuZn25. However, this downward trend primarily reflects a change in the specific capacitance of the material rather than a geometric reduction in available surface atoms. In our kinetic model Γ represents the areal concentration of sites capable of CO_2 activation. The identified increase in Γ suggests that while the macroscopic capacitance decreases due to shifting electronic properties of the double layer, Zn alloying activates a higher fraction of the surface Cu atoms for CO_2 adsorption. Crucially, this increase in Γ alone cannot explain the enhanced activity with Zn content. As demonstrated in our sensitivity analysis (Figures S22 and S23), increasing only the areal concentration of active sites reproduces higher currents but simultaneously suppresses the characteristic hysteresis observed in the CV experiments (Figure 1).

In summary, the contradictory trends for Cases A and B regarding the impact of Zn suggest fundamentally different mechanistic explanations for the enhanced activity of CuZn alloys. Case A emphasizes the role of Zn in the CO_2 activation step, while Case B emphasizes the role of Zn on the formation and desorption of CO. To further evaluate these hypotheses, we carry out a detailed analysis of rates and coverages for both Cases, followed by DFT calculations to clarify Zn's mechanistic role at the atomistic level.

2.2.1 | *Case A*

Case A provides an excellent match to the experimental data and, therefore, is a plausible explanation for the observed enhancement in electrocatalytic activity with increasing Zn content. To gain a deeper mechanistic understanding of the predicted underlying kinetic improvements, we conducted a detailed kinetic analysis of Case A. This analysis focuses on examining the evolution of adsorption and desorption rates, reaction rates, as well as surface coverages of intermediates as functions of the applied potential during dynamic cycling.

Figure 5a–d presents the simulated reaction and sorption rates for a scan rate of 200 mV s^{-1} for Case A. Notably, the CO_2 adsorption and reduction rates of all materials exhibit an S-shaped curve, characterized by an initial region of low activity, followed by a gradual increase starting around −1.6 V. The activity then plateaus at potentials more negative than −2.2 V. In contrast, the formation and desorption rates of CO continue to increase throughout the forward sweep. This difference in the rate profile suggests that the initial CO_2 activation steps, including CO_2 adsorption and reduction to $*CO_2^-$, are rate limiting, while the subsequent CO formation and CO desorption rates are less kinetically constrained under these conditions. In terms of the effect of the Zn content, all four reaction steps exhibit rates that increase monotonically with the Zn content, which explains the experimentally observed increase in overall catalytic activity. Only CuZn20 deviates from this trend in the CO desorption rate (Figure 5d), showing an abnormally low magnitude and pronounced hysteresis. This can be explained by the strong outlier of its CO desorption rate constant shown in Figure 4b and is confirmed by simulations using linearly interpolated parameters for CuZn20 that do not show such a deviating trend (Figure S25).

Surface coverages reveal limitations, such as blocking by prevalent species or the absence of reactants for a given reaction step; therefore, we analyze the coverages of adsorbed intermediates $*CO_2$, $*CO_2^-$, *CO, and free sites (*) during CV (Figure 5e–g). The coverage of free sites decreases significantly from Cu to CuZn10 and further to CuZn25, indicating improved catalyst utilization with increasing Zn content. This decrease may also result

1864564x, 2026, 21, Downloaded from https://chemistry-europe.onlinelibrary.wiley.com/doi/10.1002/cssc.70800 by Karlsruher Institut Fur Technologie, Wiley Online Library on [10/11/2026]. See the Terms and Conditions (https://onlinelibrary.wiley.com/terms-and-conditions) on Wiley Online Library for rules of use; OA articles are governed by the applicable Creative Commons License

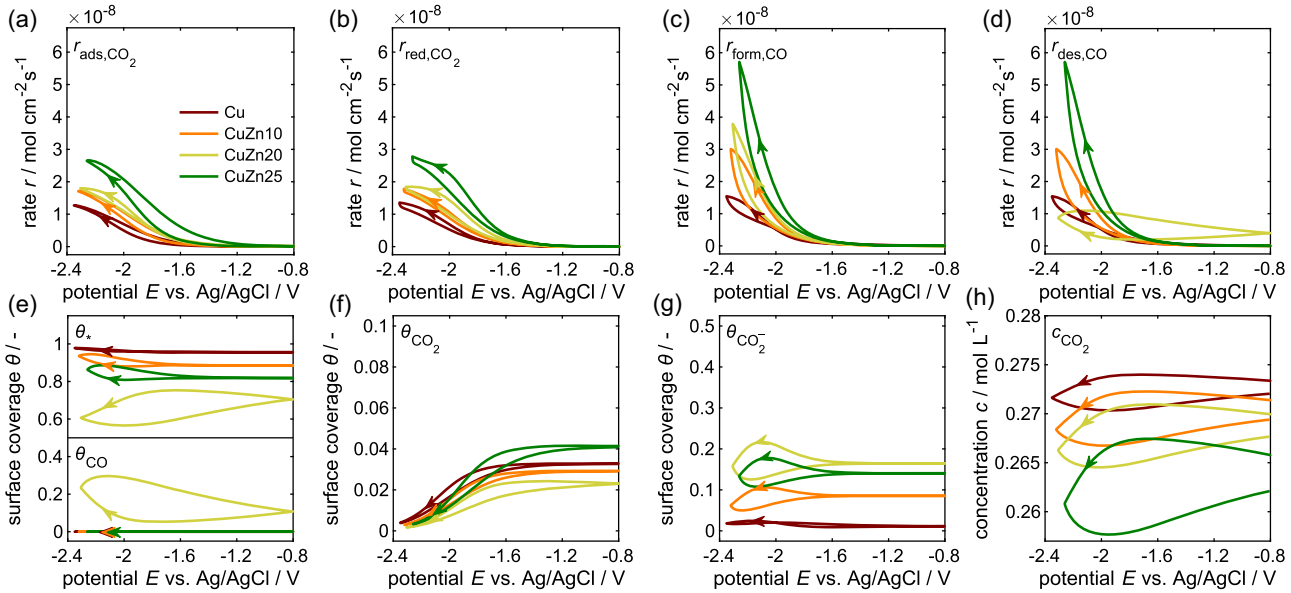


FIGURE 5 | Simulated reaction rates and surface coverages during CV at 200 mV s^{-1} for Cu and α-CuZn electrocatalysts based on Case A: (a) CO_2 adsorption rate, (b) CO_2 reduction rate, (c) CO formation rate, (d) CO desorption rate, (e) free surface site coverage (*) (upper part) and adsorbed CO coverage (*CO) (lower part), (f) adsorbed CO_2 coverage (*CO_2), (g) adsorbed CO_2 radical anion coverage (*CO_2^-), and (h) concentration of dissolved CO_2 at the electrode–electrolyte interface.

from site blocking by strongly adsorbed intermediates, which could limit the overall activity. Again, CuZn20 exhibits the most pronounced decrease in free sites but displays a distinct profile and is therefore considered an outlier, as discussed previously.

CO_2 coverage (θ_{CO_2}) is generally low (below 5 %) and drops sharply to almost zero at potentials below −1.6 V, suggesting that the supply of *CO_2 by adsorption is smaller than its consumption in the subsequent step, i.e., the adsorption of CO_2, is rate limiting at high cathodic potentials, not only for Cu [38] but also for the CuZn alloys.

The coverage of *CO_2^- is significantly increased for the CuZn alloys compared to pure Cu. It increases with Zn content (with CuZn20 as an outlier) and correlates with the observed increase in CO_2RR activity with increasing Zn content. The increased *CO_2^- coverage in the α-CuZn alloys may be attributed to a stabilizing effect of the Zn alloy environment on *CO_2^-, as Zn is more oxyphilic than Cu [58]. Furthermore, the presence of Zn sites neighboring Cu steps has been reported to facilitate CO_2 activation in thermal catalysis [31].

Our simulations of Case A predict negligible *CO coverage across the potential range studied for Cu, CuZn10, and CuZn25. This aligns with Fourier transform infrared spectroscopy (FTIR) studies of polycrystalline Cu, which reported the absence of infrared bands characteristic of adsorbed CO in acetonitrile electrolyte [14, 59]. CuZn20 is denoted as an outlier due to its significantly higher CO desorption rate constant.

To confirm the absence of mass transport limitations, the concentration profiles of dissolved CO_2 at the electrode–electrolyte interface are given in (Figure 5h). CO_2 concentration decreases at potentials below −2 V, with lower concentrations, indicating higher consumption rates, observed for alloys with higher Zn content. The slight increase in concentration from −0.8 to −2 V can be attributed to the slow diffusion of CO_2 from the bulk, which replenishes the consumed CO_2 during phases of low current density. Despite the high CO_2 consumption rates, the CO_2 concentration at the electrode remains above 92% of its saturation value throughout the potential window, indicating that mass transport limitations are negligible under the conditions studied. This conclusion is further supported by the nearly perfect overlap of consecutive simulated CV cycles with minimal drift. Furthermore, our experimental CVs recorded at scan rates between 50 and 300 mV s^{-1} demonstrate that the cathodic current continues to increase with scan rate and does not converge to a scan rate-independent limiting current characteristic of a diffusion-controlled regime (Figures S4–S7). This conclusion is also consistent with previous work on Cu in the same electrolyte, which found no CO_2 depletion at the Cu surface under comparable conditions [38], and with McGregor's studies on similarly active Ag electrodes in aprotic media, where transport limitations were also ruled out. Steady-state simulations extended to potentials beyond −2.4 V further confirm that the depletion of dissolved CO_2, and thus a transport-limited current, does not occur for the planar CuZn electrodes (Figure S21). However, for structured electrodes with a high specific area, such as meshes or nanoparticle-based catalysts, transport limitations may arise, as shown in Figure S21.

In summary, for Case A, the improvements in the rates observed for the higher alloyed α-CuZn catalysts can be primarily attributed to an improvement in CO_2 activation. The observed increase in both CO_2 adsorption and CO_2 reduction rates, coupled with the enhanced coverage of *CO_2^-, suggests that Zn alloying facilitates the initial steps of the CO_2 reduction pathway. The increased coverages do not appear to displace other adsorbed species, indicating improved utilization of the available sites.

1864564x, 2026, 21, Downloaded from https://chemistry-europe.onlinelibrary.wiley.com/doi/10.1002/cssc.70800 by Karlsruher Institut Fur Technologie, Wiley Online Library on [10/11/2026]. See the Terms and Conditions (https://onlinelibrary.wiley.com/terms-and-conditions) on Wiley Online Library for rules of use; OA articles are governed by the applicable Creative Commons License

2.2.2 | *Case B*

Case B contains significantly different kinetic parameters and therefore may offer an alternative mechanistic explanation for the enhanced electrocatalytic activity observed in α-CuZn alloys.

The calculated reaction rates (Figure 6a–d) show that all steps exhibit increased rates with higher Zn content, mirroring the trends observed in Case A. The most significant increases with Zn content are observed in the CO_2 reduction and CO formation rates, suggesting that Zn facilitates electron transfer in both these steps. The rates of CO_2 adsorption and CO desorption exhibit less pronounced increases. Furthermore, compared to Case A, the CO desorption rate is slower, indicating that the desorption of CO may limit CO_2RR.

The corresponding surface coverages (Figure 6e–h) exhibit significant differences compared to Case A. The percentage of free sites is considerably lower across the CuZn alloy series, remaining below 20 % and approaching near-zero values at potentials more negative than −2 V, with the exception of CuZn20, which again displays anomalous behavior. The coverage of CO_2 is significantly higher compared to Case A, but also decreases at potentials more negative than −1.8 V, approaching zero between −2.4 and −2.5 V. This indicates that, in addition to CO desorption, CO_2 adsorption also contributes to slow CO_2 reduction kinetics.

$*CO_2^-$ is absent from the surface at high Zn content, i.e., CuZn20 and CuZn25, indicating that it reacts more rapidly than it is produced. However, at low Zn content, i.e., CuZn10 and Cu, a significant amount of adsorbed $*CO_2^-$ accumulates, which rapidly disappears at potentials below −2.0 V.

Finally, the CO coverage shows the most significant difference compared to Case A. While CO coverage was negligible in Case A, Case B predicts a rapid increase in CO coverage to approximately 80% below −1.6 V. This substantial CO coverage at elevated cathodic potentials, coupled with the fact that the estimated parameter value for the areal concentration of adsorption sites Γ in Case B is one order of magnitude smaller compared to Case A, suggests saturation of the surface with adsorbed CO during CO_2RR. This effectively blocks a large fraction of the catalyst surface and limits the available sites for further CO_2 conversion. Although the accumulation of CO on the surface is observed in all materials, higher alloyed CuZn materials appear to partially mitigate this effect through enhanced CO desorption rates. Furthermore, the complete removal of adsorbed CO during the anodic scan suggests that the high coverage by *CO stems from CO formed by CO_2RR rather than re-adsorption from solution. The high CO coverage predicted contrasts with the aforementioned reports of low CO coverage of Cu in acetonitrile by FTIR spectroscopy [14, 59]. However, experimental uncertainties due to the low sensitivity of FTIR for detecting CO bands in acetonitrile. In contrast, in aqueous electrolytes, Cu typically exhibits distinct IR bands for adsorbed CO species during CO_2RR [60].

In summary, Case B suggests that the catalytic performance of Cu and CuZn alloys is limited by the saturation of the surface with CO exceeding 80 % coverage. Although Zn may facilitate the electron transfer reactions, as evidenced by the enhanced CO_2 reduction and CO formation rates, the primary mechanism for the improved activity of CuZn alloys, according to Case B, is the improved removal of adsorbed CO at elevated potentials.

2.2.3 | *Assessing Adsorbed CO Accumulation*

To assess the likelihood of CO poisoning, and thus of Case B, we performed CV experiments in CO-saturated and 50:50 (v/v) CO:CO_2-saturated electrolyte on Cu and CuZn25. The experimental

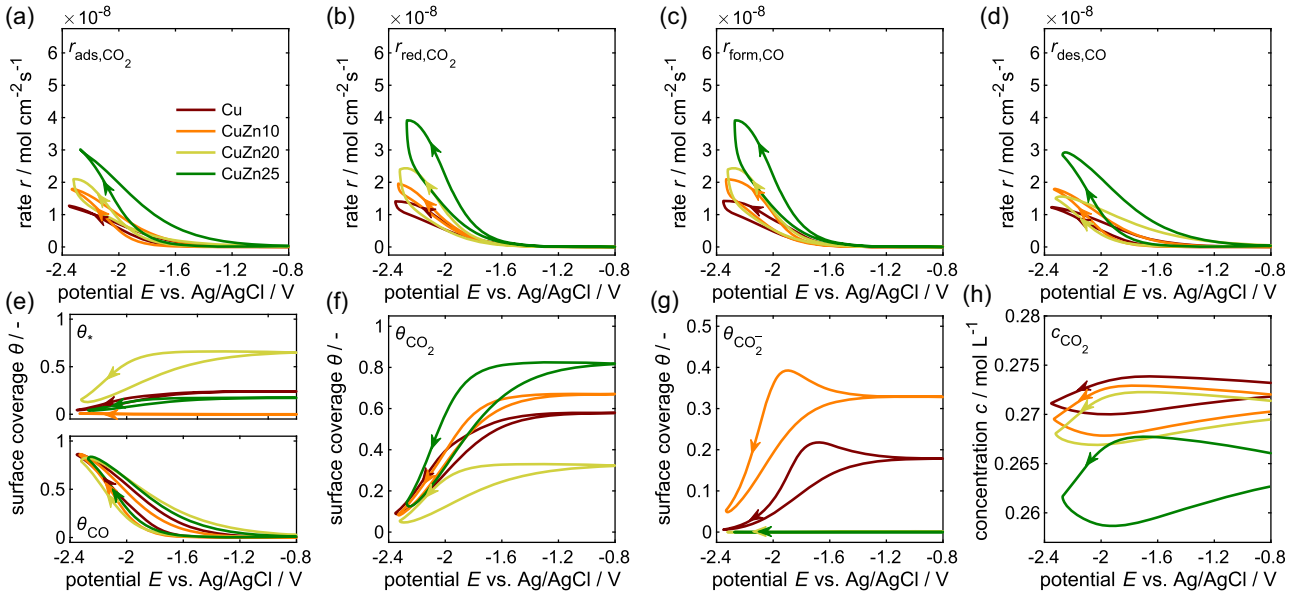


FIGURE 6 | Simulated reaction rates and surface coverages during CV at 200 mV s^{-1} for Cu and α-CuZn electrocatalysts based on Case B: (a) CO_2 adsorption rate, (b) CO_2 reduction rate, (c) CO formation rate, (d) CO desorption rate, (e) free surface site coverage (*) (upper part) and adsorbed CO coverage (*CO) (lower part), (f) adsorbed CO_2 coverage ($*CO_2$), (g) adsorbed CO_2 radical anion coverage ($*CO_2^-$), and (h) concentration of dissolved CO_2 at the electrode–electrolyte interface.

1864564x, 2026, 21, Downloaded from https://chemistry-europe.onlinelibrary.wiley.com/doi/10.1002/cssc.70800 by Karlsruher Institut Fur Technologie, Wiley Online Library on [10/11/2026]. See the Terms and Conditions (https://onlinelibrary.wiley.com/terms-and-conditions) on Wiley Online Library for rules of use; OA articles are governed by the applicable Creative Commons License

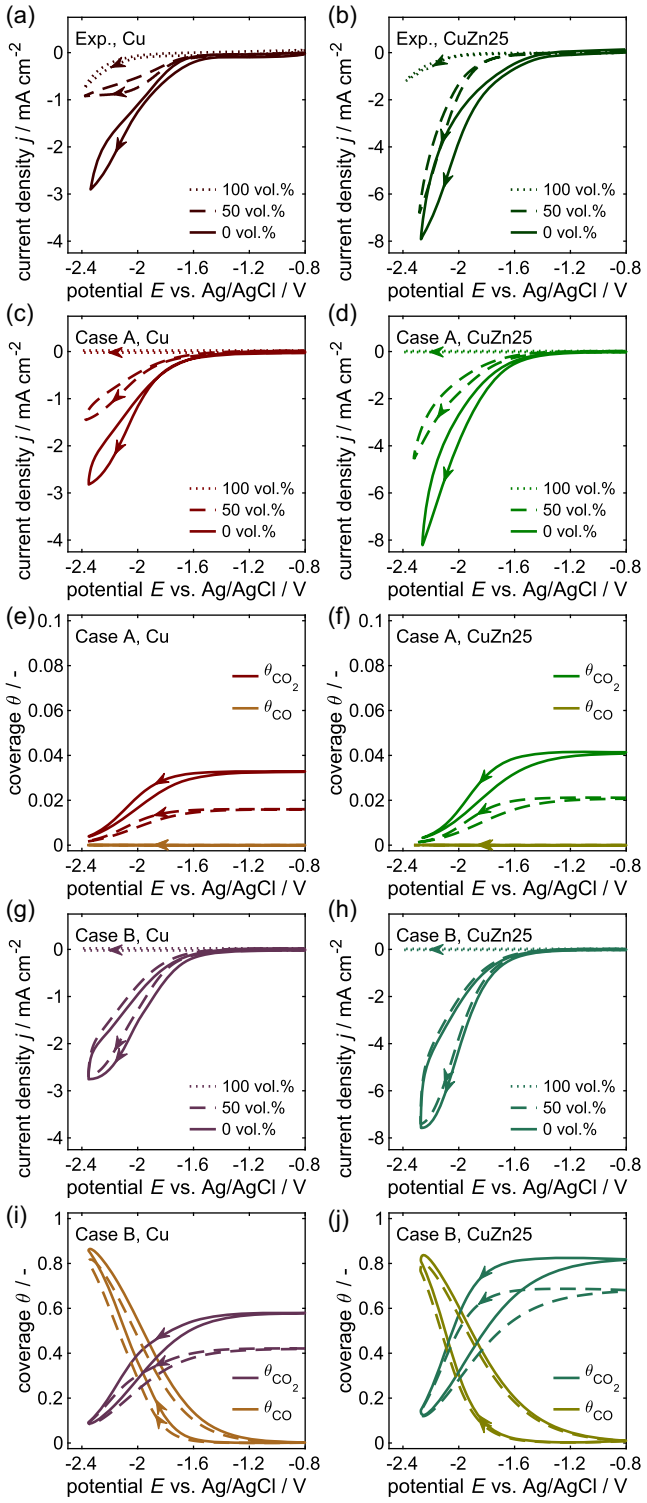


FIGURE 7 | Experimental and simulated CVs and corresponding surface coverages on Cu and CuZn25 electrodes in aprotic 0.1 mol L^{-1} $TBABF_4$ acetonitrile electrolyte at room temperature and a scan rate of 200 mV s^{-1} under CO atmosphere (100 vol.% CO), 50:50 (v/v) CO/CO_2 atmosphere (50 vol.% CO), and CO_2 atmosphere (0 vol.% CO). Panels (a) and (b) show experimental CVs for Cu and CuZn25, respectively, panels (c) and (d) show Case A simulated CVs, and panels (g) and (h) show Case B simulated CVs. Panels (e) and (f) show Case A simulated surface coverages of θ_{CO_2} and θ_{CO} for Cu and CuZn25, respectively, while panels (i) and (j) show the corresponding coverages for Case B.

results are shown in Figure 7 along with the corresponding simulations based on Cases A and B.

In the absence of CO_2, i.e., 100 vol.% CO atmosphere, the CVs of Cu and CuZn25 exhibit negligible reduction currents until cathodic potentials below −2.0 V, where minor activity likely arises from the decomposition of acetonitrile rather than CO reduction, as there is no proton source [61]. We do not explicitly include electrolyte decomposition in the kinetic model, because the acetonitrile decomposition kinetics and pathway is highly complex as it depends on the gas atmosphere, e.g., for Ar- and CO_2-saturated conditions (for Ar CVs, see Figure S29) [22]. As such, the CVs cannot be corrected by subtracting the Ar contribution from the full spectrum. Consequently, simulations for both catalysts predict no activity in this regime. Although electrolyte decomposition may overlap with the measurements under CO_2 atmosphere at potentials below −2.0 V, additional analysis shows that the mechanistic conclusions of our kinetic model remain unchanged even when accounting for acetonitrile reduction. As detailed in Section S11, the kinetic parameters for Case A were re-parameterized using background-corrected data, which was obtained by subtracting the CVs recorded under 100 vol.% CO from the original CO_2 CVs. This reevaluation yielded the same mechanistic interpretation and kinetic trends as the original model (see Figures S26–S28), confirming that our conclusions are robust with respect to potential electrolyte decomposition.

The 50:50 (v/v) $CO:CO_2$ experiment shows no clear evidence of CO poisoning on CuZn25; the observed current density was approximately 14% lower compared to CO_2 atmosphere. This is attributed to the reduced CO_2 partial pressure and, thus, CO_2 concentration, although a shift in the onset to more negative potentials is observed. In contrast, Cu shows a more substantial decrease in current density under 50:50 (v/v) $CO:CO_2$ conditions. This may be attributed to CO poisoning or to the lower CO_2 concentration, which has a stronger effect on CO_2 adsorption on pure Cu. CO poisoning is unlikely here as well, as molecular dynamics simulations showed facile CO desorption from Cu into bulk acetonitrile solution [62].

Simulations confirm that Case A reproduces the 50:50 (v/v) $CO:CO_2$ experiment much better, while Case B fails to reproduce the experimental trend. As shown in Figure 7e and f, Case A captures the observed gas-composition dependence of the CV via reduced CO_2 coverage, i.e., lower θ_{CO_2}, rather than changes in CO coverage, and shows no signs of CO poisoning, as θ_{CO} remains negligible for all gas mixtures. In contrast, the simulated CVs based on Case B are largely insensitive to variations in CO and CO_2 concentrations, contradicting the experiments and thus rendering the parameter set of Case B implausible.

3 | Density Functional Theory Results: Potential-Dependent Adsorption

To corroborate the indications from the kinetic analysis favoring Case A over Case B for the observed enhancement in CO_2 reduction activity, we performed DFT calculations probing CO_2 and CO adsorption energies on Cu(111) and $Cu_3Zn(111)$ surfaces. We chose the $Cu_3Zn(111)$ surface as a representative model

1864564x, 2026, 21, Downloaded from https://chemistry-europe.onlinelibrary.wiley.com/doi/10.1002/cssc.70800 by Karlsruher Institut Fur Technologie, Wiley Online Library on [10/11/2026]. See the Terms and Conditions (https://onlinelibrary.wiley.com/terms-and-conditions) on Wiley Online Library for rules of use; OA articles are governed by the applicable Creative Commons License

TABLE 3 | DFT-calculated Gibbs free energies ΔG_{ads} at 298.15 K of CO_2 and CO adsorption on the top sites in vacuum.

Surface	Site	ΔG_{ads}, eV	
		$*CO_2$	*CO
Cu(111)	Cu	+0.19	−0.02
Cu_3Zn(111)	Cu	+0.25	+0.16
	Zn	+0.34	+0.65

for the α-CuZn alloy surfaces as this provides a reasonable model with $\frac{1}{4}$ Zn atoms in the first surface layer. We also note that we expect Zn to be present in the surface layer due to its segregation energy in copper (see Figure S13).

The free energies of adsorption are shown in Table 3 (enthalpies, see Table S2). CO_2 is physisorbed on all investigated sites with a metal–carbon distance above 3.5 Å and an O—C—O angle of 180°. In contrast, CO is chemisorbed at the on-top sites on Cu with a metal–carbon distance of 1.9 Å. On Zn sites, CO exhibits weaker adsorption (physisorbed), characterized by an elongated metal–carbon distance (>2.1 Å). Additional analysis of the dispersion contribution to the adsorption energies further supports this conclusion (Table S3). This suggest that CO potentially blocks the surface of pure Cu, seemingly consistent with Case B of our kinetic modeling, whereas for the Cu_3Zn alloy, such a problem should not arise. Indeed, the calculated coverage difference derived from the corresponding free-energy differences amounts to about three orders of magnitude between Cu and Cu_3Zn (refer to the Supporting Information).

To move toward a more realistic description of the electrochemical interface, sawtooth slab calculations were performed (see Supporting Information for details). These preliminary results indicate that Zn exhibits a stronger affinity toward the oxygen atoms of CO_2, leading to a reduced adsorbate–surface distance. This may enhance the reduction rate by increasing the orbital overlap between the electrode states and CO_2. However, no true chemisorbed state is observed in this simplified vacuum model as the interaction remains strictly governed by dispersion forces (Table S3). This absence of spontaneous chemisorption, contrary to experimental observations, indicates that a more complete representation of the electrochemical interface is required to accurately capture the active state.

3.1 | Grand Canonical Approach

The simulations in vacuum are a rather simplified model of an electrochemical interface. A step toward improving this approach is to include an implicit solvent and explicitly charge the interface. As a result, GC adsorption energies, i.e., the constant-potential free energy Ω, of CO_2 and CO were obtained (Figure 8).

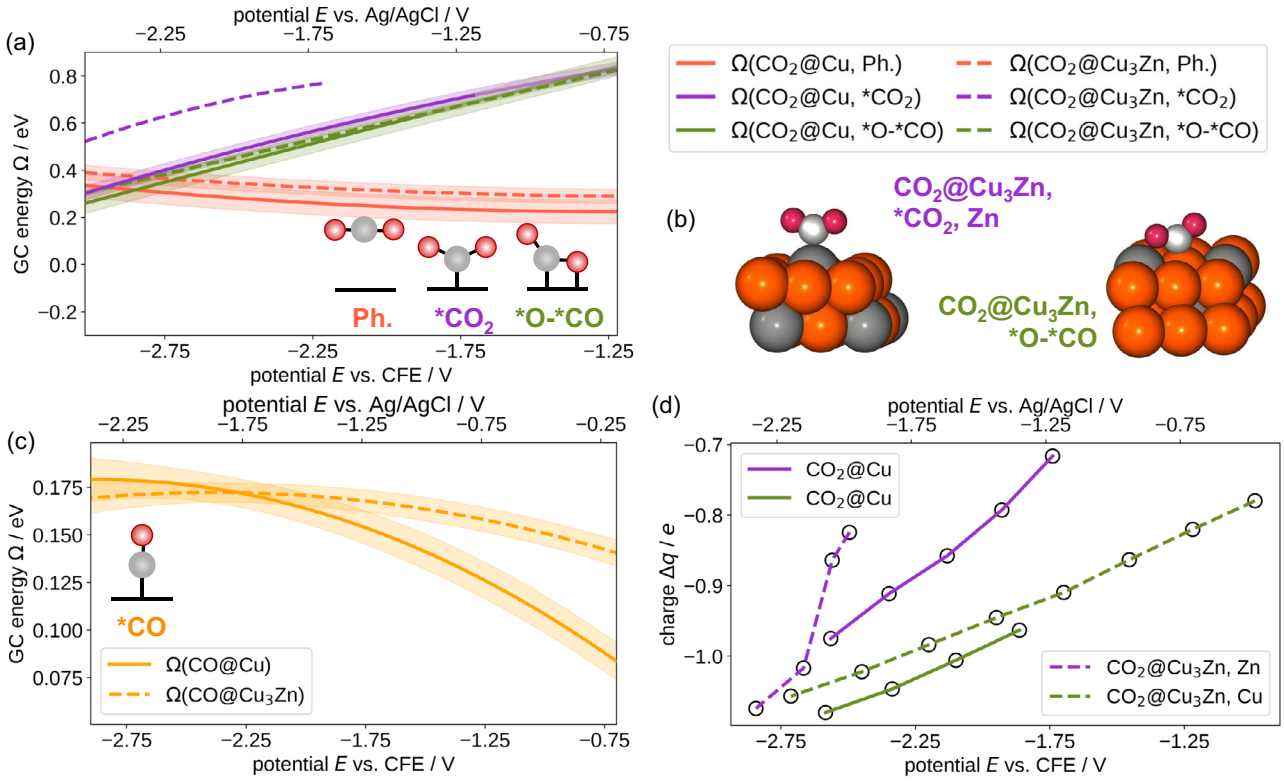


FIGURE 8 | VASPsol Results. (a,c) GC adsorption energies of CO_2 and CO on Cu and Cu_3Zn surfaces. The insets schematically show the main modes of adsorption (Ph.: physisorbed). The upper *x*-axis indicates the potential values versus Ag/AgCl, derived from the experimentally determined ferrocene redox potential. The light sections of the lines indicate regions where this type of adsorption has not been observed. 2σ confidence intervals shown as shaded regions. (b) Structure of chemisorbed CO_2 on Cu_3Zn (the slab was truncated for clarity). (d) Transferred charge Δq to the CO_2 molecule in the chemisorbed state as a function of the applied potential on both surfaces, obtained with Bader charge analysis.

1864564x, 2026, 21, Downloaded from https://chemistry-europe.onlinelibrary.wiley.com/doi/10.1002/cssc.70800 by Karlsruher Institut Fur Technologie, Wiley Online Library on [10/11/2026]. See the Terms and Conditions (https://onlinelibrary.wiley.com/terms-and-conditions) on Wiley Online Library for rules of use; OA articles are governed by the applicable Creative Commons License

The presence of the solvent stabilizes the chemisorbed state on the surface, characterized by a reduction of the O–C–O angle to 130° and a decrease in the distance between the surface and the molecule to 2.1 Å. This chemical binding can occur either through a single C—M bond or through two bonds, C—M and O—M, giving rise to two chemisorption modes of CO_2, denoted as $*CO_2$ and *O-*CO, respectively, as shown in the inset of Figure 8a. This observation is consistent with previous reports for aqueous electrochemical environments [63]. In both Cases, the stabilization is caused by the charge transferred from the slab to CO_2, making it negatively charged. The transferred charge Δq therefore depends on the applied potential (Figure 8d).

Based on the assumption that electroactivation (in this Case, chemisorption) of CO_2 is the rate-limiting step of electroreduction [64, 65], we therefore consider the intersection between the physisorbed and chemisorbed states as the upper limit of onset potential for CO_2 activation. This yields the intersection potentials of −2.43 and −2.33 V versus Ag/AgCl for Cu, and −2.72 and −2.27 V versus Ag/AgCl for Cu_3Zn, corresponding to the one-bond and two-bond modes, respectively. While this observation of CO_2 activation is consistent with Case A, the calculated difference between Cu and Cu_3Zn is within the error of DFT, giving no clear trend.

Moreover, although the one-bond adsorption mode of CO_2 on Cu_3Zn reaches its intersection potential relatively late, it becomes more favorable than all other modes at very high overpotentials (Figure 8a). This additional adsorption mode could further enhance the CO_2RR rate at very negative potentials. An additional advantage of this scenario is that CO does not adsorb on zinc, which enables the rapid release of the reduction product and provides access for new CO_2 molecules.

CO adsorption exhibits a slightly more pronounced curvature on the Cu surface (Figure 8c), with the adsorption energy of CO displaying a convex parabolic behavior in agreement with Cheng et al. [66]. At relevant cathodic potentials, below −1.6 V versus Ag/AgCl, the adsorption energies remain comparable between Cu and Cu_3Zn with an average difference of 0.02 eV, indicating that alloying has a negligible influence on CO binding and desorption, and thus cannot explain the activity enhancement proposed by Case B. We note that another recent study reports an opposite curvature of CO adsorption energetics [67], where CO adsorption initially stabilizes with increasingly negative potential before destabilizing again. These contrasting reports suggest that our CO adsorption results should be interpreted with caution.

Nevertheless, we can estimate the contributions to the enhancement of CO_2RR from CO_2 activation and CO desorption by calculating the difference between the adsorption energy curves on Cu_3Zn and Cu surfaces as $\Delta\Omega(CO_2/CO) = \Omega(CO_2/CO@Cu_3Zn) - \Omega(CO_2/CO@Cu)$ for CO_2 and CO, respectively (Figure 9), where the *O–*CO configuration is used for $\Omega(CO_2@Cu)$, as it is the most favorable conformation on Cu. As shown in Figure 9, the difference in the CO_2 adsorption energetics is slightly more pronounced over a broad potential range, although no strong effect of Zn is observed, whereas the corresponding changes in CO adsorption remain small.

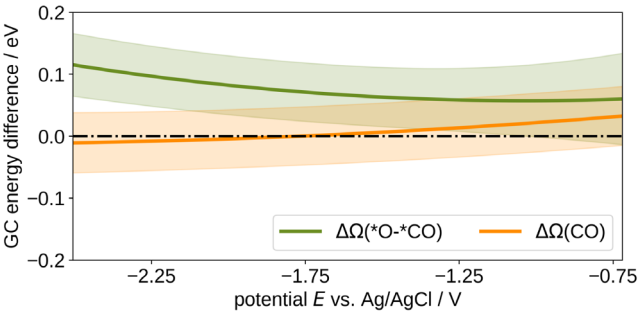


FIGURE 9 | GC adsorption energy difference for CO_2 and CO on Cu_3Zn versus the most stable conformation on Cu, namely the two-bond chemisorption of CO_2 and on-top adsorption of CO. The same color scheme as in Figure 8 is used.

4 | Conclusion

This study presented a comprehensive investigation of α-CuZn alloy catalysts for CO_2 electroreduction in an aprotic acetonitrile-based electrolyte, combining electrochemical experiments, kinetic modeling, and DFT calculations to unravel the role of Zn in enhancing catalytic performance.

Experimental cyclic and LSV measurements demonstrated a significant increase in catalytic activity with increasing Zn content in the α-CuZn alloys, with CuZn25 exhibiting the highest current density across all measurement conditions. This enhancement was accompanied by a shift in the onset potential toward more positive potentials and pronounced hysteresis, indicating the involvement of adsorbed reaction intermediates. The performance of pure Zn, by contrast, remained poor, with a delayed onset and lower currents, suggesting that Zn acts as a promoter when alloyed with Cu rather than as an independent active site.

To interpret these trends, we applied a dynamic kinetic model describing CO_2 activation, electron transfer, and product desorption steps. Two plausible mechanistic Cases were identified. In Case A, Zn was found to enhance CO_2 activation by increasing the rate of the initial electron transfer step to $*CO_2^-$. This Case predicted improved reaction rates and intermediate coverages in agreement with experimental observations. In Case B, the model attributed the activity enhancement primarily to facilitated CO desorption. However, it also predicted excessive CO coverage that was inconsistent with spectroscopic and molecular dynamics simulation studies.

Finally, DFT calculations provided atomistic support for Case A over Case B by demonstrating that Zn incorporation into the Cu lattice stabilizes CO_2 chemisorption to CO_2^- at lower overpotentials, while showing similar CO adsorption energies for Cu and Cu_3Zn at relevant cathodic potentials. A bidentate binding configuration of CO_2 was identified as the most stable at intermediate potentials. At elevated overpotentials, a further monodentate binding mode located on Zn has been identified.

Case A is therefore favored over Case B based on the combined agreement with CV hysteresis, scan-rate dependence, CO atmosphere experiments, and DFT adsorption energetics. While Case B predicts excessive CO accumulation and weak gas-composition

1864564x, 2026, 21, Downloaded from https://chemistry-europe.onlinelibrary.wiley.com/doi/10.1002/cssc.70800 by Karlsruher Institut Fur Technologie, Wiley Online Library on [10/11/2026]. See the Terms and Conditions (https://onlinelibrary.wiley.com/terms-and-conditions) on Wiley Online Library for rules of use; OA articles are governed by the applicable Creative Commons License

dependence that are not observed experimentally, Case A correctly attributes the promotional effect of Zn to facilitated CO_2 activation.

The combined experimental, kinetic, and computational insights presented here establish a coherent mechanistic understanding of Zn promotion in CuZn alloys. While this advancement improves CO_2 activation, CO_2 adsorption remains relatively slow, limiting overall rates and suggesting opportunities for further system optimization that combine Zn-promoted Cu alloys with high-surface-area architectures or elevated CO_2 pressures.

5 | Experimental Section

5.1 | Electrode Preparation

CuZn electrodes were prepared by machining commercially purchased metal rods into planar disk electrodes; no alloy synthesis was performed in-house. Cu and Zn rods (both 99.99%, Thermo Fisher Scientific Inc.) and α-brass metal rods with Zn mass contents of 10%, 20% and 25% (99.99%, Rich Special Materials Co., Ltd.) were used. The metal rods were lathed to a uniform diameter of 5 mm and cut into cylindrical pieces with a height of 4 mm. For initial preparation, the top side of the disk electrode was sanded with 2000-grit SiC paper and sequentially polished with 9, 3, and 1 µm water-based diamond suspensions (Struers GmbH). Afterward, the disks were mounted in PEEK shrouds (E5TQPK, Pine Research Instrumentation, Inc.). To minimize the influence of surface oxidation and remove the native oxide layer, the disk electrodes were freshly polished before each measurement with 0.25 µm diamond paste (Kemet International Ltd.), rinsed with ultrapure water, ultrasonicated for 5 min in ultrapure water, rinsed again with ultrapure water, and finally dried by blowing them with compressed air.

5.2 | Electrochemical Measurements

Measurements were conducted in a 250-mL three-electrode glass cell setup equipped with a Ag/AgCl (KCl_{sat} in H_2O) reference electrode (Sensortechnik Meinsberg) and a Pt-coil counter electrode (∅ 0.5 mm, Heraeus Precious Metals GmbH & Co. KG) (Figure S2). A volume of 150 mL electrolyte solution consisting of 0.1 mol L^{-1} tetrabutylammonium tetrafluoroborate ($TBABF_4$) in acetonitrile was prepared using $TBABF_4$ (98 %, abcr GmbH) and acetonitrile (≥ 99.9 % max. 100 ppm H_2O, VWR Chemicals). To ensure thermodynamic consistency in the aprotic electrolyte, the Ag/AgCl reference electrode was calibrated against the ferrocene/ferrocenium (Fc^0/Fc^+) redox couple (see Figure S3). The electrolyte was saturated with CO_2 gas (≥99.995%, Air Liquide Deutschland GmbH) by bubbling at a constant flow rate of 60 mL min^{-1} for 15 min through a fritted bubbler directly before the measurements. During the measurements, a CO_2 gas atmosphere was maintained in the headspace above the solution by using a bypass flow of CO_2 gas in the headspace at a rate of 30 mL min^{-1}. For the CO and Ar experiments, CO gas (≥99.5%, Air Liquide Deutschland GmbH) or Ar gas (≥99.999%, Air Liquide Deutschland GmbH) was used, respectively, to saturate the electrolyte solution and headspace, following the same procedure as for CO_2. At the start of each measurement, a preconditioning step consisting of 20 consecutive CV cycles recorded at 100 mV s^{-1} between −0.8 and −2.4 V versus Ag/AgCl was performed. This procedure serves to stabilize the interface and minimize the influence of residual water. Subsequently, CV measurements were conducted at scan rates of 300, 200, 150, 100, 75, and 50 mV s^{-1} in descending order. LSV was performed directly afterward at a scan rate of 1 mV s^{-1}. For both CV and LSV, the potential range was set from −0.8 to −2.4 V versus Ag/AgCl to avoid electrode oxidation and electrolyte degradation. As we observed no transport limitation in our previous study [38], no rotation was applied. All electrochemical measurements were performed at ambient conditions (25 °C, 101.3 kPa) using a Gamry Interface 1010E potentiostat and were repeated three times in total on the same electrode. For each repetition, fresh electrolyte solution was used, and the electrode was freshly polished using 0.25 µm diamond paste, cleaned, and dried as described above. After the preconditioning step, the uncompensated resistance R_u was determined by identifying the high-frequency resistance (100 kHz to 1 MHz, phase angle $\varphi = 0°$) using potentiostatic EIS at −0.8 V with an input amplitude of 10 mV. Post-run *iR* correction was applied to all data.

6 | Computational Methods

6.1 | Kinetic Model Details

6.1.1 | *Model Description*

The dynamic kinetic model describes the processes at the cathode half-cell during CO_2RR at a planar electrode immersed in a stagnant, CO_2-saturated 0.1 mol L^{-1} $TBABF_4$ acetonitrile electrolyte at room temperature and atmospheric pressure. Consistent with previous reports on Cu and α-CuZn catalysts in acetonitrile, which show high selectivity toward CO with only trace oxalate formation [37], the model assumes that the measured Faradaic current is dominated by the CO_2-to-CO pathway. This is further supported by our control measurements in Argon (Figure S29), which exhibit significantly lower current densities than those recorded under CO_2. To capture the influence of concentration gradients and mass transport within the simulation domain, the model contains one-dimensional diffusive transport of CO, CO_2, and CO_3^{2-} within the electrolyte's Nernst diffusion layer between the electrode surface and the ideally mixed bulk electrolyte. At the electrode, reactions, adsorption, and desorption processes occur, as detailed in our previous work [38]. All calculations were performed using the ode15s solver in MATLAB 2024b.

In our previous microkinetic modeling study of the oxygen evolution reaction (OER) on binary Ir–Ru catalysts, two distinct active sites were assumed because both Ir and Ru exhibited significant OER activity as pure metal oxides and showed distinct characteristic CV features [41]. In contrast, for the CO_2RR on CuZn alloys, Zn alone shows no activity above −2.0 V (see Figure 1), and both Cu and Zn individually exhibit lower activity than the CuZn alloys. Therefore, the catalytic behavior of the CuZn alloys cannot be described as a linear combination of Cu and Zn, indicating a synergistic promoting effect. Since the CV profiles of the CuZn alloys closely resemble those of pure

1864564x, 2026, 21, Downloaded from https://chemistry-europe.onlinelibrary.wiley.com/doi/10.1002/cssc.70800 by Karlsruher Institut Fur Technologie, Wiley Online Library on [10/11/2026]. See the Terms and Conditions (https://onlinelibrary.wiley.com/terms-and-conditions) on Wiley Online Library for rules of use; OA articles are governed by the applicable Creative Commons License

Cu, albeit with enhanced activity, our modeling approach considers only Cu sites on the surface to be active for CO_2RR, while Zn's role is incorporated indirectly through its influence on the kinetic parameters. This approach provides valuable insights into surface coverages and thus represents an important first step in the kinetic modeling of this system.

We adopted the mechanism proposed by Amatore and Savéant with the following simplification [38, 68]: CO_2 attachment to the radical anion, subsequent electron transfer, and carbonate detachment are treated as a single effective step. For this process, the model thus utilizes an effective step representation rather than a fully elementary description as the carbonic formic anhydride radical anion is not resolved as a separate intermediate. This is justified because the species has not been experimentally confirmed and is therefore considered a short-lived transition state. The implemented reaction mechanism thus consists of the following steps

1. CO_2 adsorption: Reversible adsorption of CO_2 on free active surface sites of the catalyst (∗).

$$CO_2 + * \underset{}{\overset{r_{ads,CO_2}}{\rightleftharpoons}} *CO_2 \quad \text{(I)}$$

2. CO_2 reduction: Electron transfer from the electrode to adsorbed $*CO_2$ forming the $*CO_2^-$ radical anion.

$$*CO_2 + e^- \xrightarrow{r_{red,CO_2}} *CO_2^- \quad \text{(II)}$$

3. Electrochemical disproportionation: Electrochemical reduction of $*CO_2^-$ and a nearby solution-phase CO_2 to form *CO and CO_3^{2-}.

$$*CO_2^- + CO_2 + e^- \xrightarrow{r_{form,CO}} *CO + CO_3^{2-} \quad \text{(III)}$$

4. CO desorption: Desorption of *CO from the electrode surface.

$$*CO \underset{}{\overset{r_{des,CO}}{\rightleftharpoons}} CO + * \quad \text{(IV)}$$

Electrochemical reaction steps are assumed to be irreversible as no positive currents were observed in the potential range studied. Previous studies have suggested that the initial step in CO_2 activation involves the direct conversion of CO_2 from solution to the adsorbed $*CO_2^{\delta-}$, bypassing the formation of an uncharged $*CO_2$ adsorbate [25, 68, 69]. This is also supported by our DFT calculations, which show that only upon the application of a sufficiently negative potential, CO_2 chemisorbs in the form of $*CO_2^{\delta-}$ (Figure 8a,d). Recognizing that the activation of CO_2 involves a shared electron density between CO_2 and the electrode surface, we chose to model the adsorption and reduction as distinct steps in this work, analogous to our previous work [38]. This simplification avoids the complexity of incorporating fractional electron transfer within our kinetic model, which would have implications for charge balance. It is important to note that the two adsorbed states of CO_2 in our model ($*CO_2$ and $*CO_2^-$) reflect different degrees of electron transfer and do not necessarily correspond to distinct physisorbed or chemisorbed states. Consequently, caution must be exercised when determining the rate-determining step if it involves either of these closely related adsorbed states.

The rate equations corresponding to the reaction and sorption processes in Equations (I)–(IV) are expressed as follows

$$r_{ads,CO_2} = k_{ads,CO_2}\, a_{CO_2}\, \theta_* - k_{des,CO_2}\, \theta_{CO_2} \quad (1)$$

$$r_{red,CO_2} = k_{red,CO_2}\, \theta_{CO_2} \exp\left(-\frac{\left(1-\alpha_{red,CO_2}\right) FE}{RT}\right) \quad (2)$$

$$r_{form,CO} = k_{form,CO}\, a_{CO_2}\, \theta_{CO_2^-} \exp\left(-\frac{\left(1-\alpha_{form,CO}\right) FE}{RT}\right) \quad (3)$$

$$r_{des,CO} = k_{des,CO}\, \theta_{CO} - k_{ads,CO}\, a_{CO}\, \theta_* \quad (4)$$

where θ_i represents the surface coverage, θ_* represents the fraction of surface area uncovered by any adsorbate, and a_i represents the local activity in the solution of species i, assumed to be ideal ($a_i = c_i/c^0$ with $c^0 = 1\,\text{Mol L}$). For the electrochemical steps, we assume irreversible Tafel kinetics relating the rate to the potential E versus Ag/AgCl at the electrode–electrolyte interface, with the Faraday constant F and the product of temperature and the universal gas constant RT. The parameters α_{red,CO_2} and $\alpha_{form,CO}$ represent the charge transfer coefficients of each electrochemical step and were treated as free, bounded optimization variables in the interval 0.1–0.9. Sensitivity analysis (Figures S22 and S23) reveals that the model is extremely sensitive to these coefficients due to their presence in the exponential term of the rate equations. The observation that these values remain nearly constant across the CuZn series suggests that the transition state symmetry for CO_2 activation is a robust characteristic of the Cu-based reaction environment that remains largely unaffected by Zn alloying. The rate equations for the electrochemical steps (Equations (2) and (3)) are expressed as functions of the electrode potential E, rather than the overpotential $\eta = E - E_{eq}$. Since the equilibrium potentials E_{eq} for the individual elementary steps are not explicitly known, the equilibrium contribution is incorporated into the effective rate constants k_i. This approach follows a well-established practice [40, 70, 71] and reduces the number of unknown parameters while accurately capturing the potential-dependent kinetic response observed in the CV experiments. Consequently, the reported values for k_i should be interpreted as effective rate constants rather than fundamental exchange rate constants.

Mass transport of reactive species in the electrolyte between the electrode surface and the bulk electrolyte is described by a one-dimensional diffusion model within the Nernst diffusion layer. Migration of carbonate in the electric field is neglected because an excess of supporting electrolyte (0.1 mol L^{-1}) is employed [72], and only low carbonate formation rates are observed. The thickness of this layer, δ, is set to 6 mm to ensure that the arising concentration gradients are fully contained within the model domain for all experimental conditions. While this value may appear large, it is important to consider that the experiments were conducted in a stagnant solution without any forced convection. Under these conditions, the diffusion layer expands continuously over time and can be estimated based on the diffusion coefficient D_i of species i and the experimental duration t using the following approximation, $\delta \approx \sqrt{D_i t}$ [73]. The species in the solution are balanced as follows

1864564x, 2026, 21, Downloaded from https://chemistry-europe.onlinelibrary.wiley.com/doi/10.1002/cssc.70800 by Karlsruher Institut Fur Technologie, Wiley Online Library on [10/11/2026]. See the Terms and Conditions (https://onlinelibrary.wiley.com/terms-and-conditions) on Wiley Online Library for rules of use; OA articles are governed by the applicable Creative Commons License

$$\frac{\partial c_{CO_2,n}}{\partial t} = D_{CO_2}\frac{\partial^2 c_{CO_2,n}(x,t)}{\partial x^2} \quad (5)$$

$$\frac{\partial c_{CO,n}}{\partial t} = D_{CO}\frac{\partial^2 c_{CO,n}(x,t)}{\partial x^2} \quad (6)$$

$$\frac{\partial c_{CO_3^{2-},n}}{\partial t} = D_{CO_3^{2-}}\frac{\partial^2 c_{CO_3^{2-},n}(x,t)}{\partial x^2} \quad (7)$$

We assume that CO_2 radical anion remains adsorbed at the electrode surface ($*CO_2^-$) and does not diffuse into the electrolyte as a solvated $CO_2^{\bullet -}$ radical anion, consistent with reports showing no detectable or, at most, only trace oxalate formation on polycrystalline Cu [14, 59, 69] and CuZn [37].

The species balance for surface species is then given by

$$\Gamma\frac{d\theta_*}{dt} = -r_{ads,CO_2} + r_{des,CO} \quad (8)$$

$$\Gamma\frac{d\theta_{CO_2}}{dt} = r_{ads,CO_2} - r_{red,CO_2} \quad (9)$$

$$\Gamma\frac{d\theta_{CO_2^-}}{dt} = r_{red,CO_2} - r_{form,CO} \quad (10)$$

$$\Gamma\frac{d\theta_{CO}}{dt} = r_{form,CO} - r_{des,CO} \quad (11)$$

with Γ referring to the areal concentration of adsorption sites. Our kinetic model does not explicitly distinguish between specific Cu and Zn sites or different crystallographic facets on the electrode surface. Instead, Γ represents all available sites, regardless of their identity, and can therefore be seen as an effective, i.e., lumped, parameter. This simplification is justified as we assume that Zn atoms are incorporated into the Cu lattice, effectively replacing Cu atoms and allowing us to treat the alloy as a homogeneous surface. Furthermore, pure Zn exhibited poor catalytic activity for CO_2 reduction, making it unsuitable as a reference for the behavior of Zn sites if we were to treat them separately.

At $t = 0$, the liquid phase is homogeneously saturated with CO_2 ($c_{CO_2,0} = 0.278\ \mathrm{mol\ L^{-1}}$) and is in equilibrium with the adsorbed CO_2 coverage, while the concentrations of CO and carbonate, as well as the surface coverages of $*CO_2^-$ and *CO, are set to zero. The bulk electrolyte boundary ($x = \delta$) is open, with constant bulk concentrations maintained by assuming perfect mixing in a large reservoir, thereby permitting bidirectional diffusive flux. The electrode boundary ($x = 0$) is impermeable to diffusion (no-flux condition) but permits all surface adsorption, reaction, and desorption processes.

Charge conservation at the electrode surface is maintained through a balance between the accumulation of charge in the electrical double layer, the total current density j_{total}, and the Faradaic current density calculated from Faraday's law

$$C_{dl}\frac{dE}{dt} = j_{total} + F\left(r_{red,CO_2} + r_{form,CO}\right) \quad (12)$$

where C_{dl} refers to the areal double-layer capacitance of the polished electrode and E refers to the local electrode potential. The total current density j_{total} is calculated via Ohm's law from the potential drop due to the uncompensated internal resistance R_u, which was measured via in situ EIS.

$$E = E_{ext} - j_{total}\,A\,R_u \quad (13)$$

The externally applied potential E_{ext} follows the temporal sawtooth profile of the respective CV experiment. By solving Equation (13) for the total current density j_{total} and substituting it into the charge balance (Equation (12)), the model couples the Ohmic losses with the interface kinetics, allowing the solver to resolve the transient interface potential E and the resulting currents.

6.1.2 | *Model Parameterization*

Separate sets for each catalyst (Cu, CuZn10, CuZn20, and CuZn25) of the following nine parameters were determined through a multistep optimization procedure using the CV measurements as described below: k_{ads,CO_2}, k_{des,CO_2}, k_{red,CO_2}, $k_{form,CO}$, $k_{des,CO}$, $k_{ads,CO}$, α_{red,CO_2}, $\alpha_{form,CO}$, and Γ.

Parameter identification was performed using a multistage global-to-local optimization strategy. Starting with Cu, a global search was conducted using MATLAB 2024b's particle swarm optimization algorithm. The initial swarm consisted of 90 randomly initialized particles, corresponding to ten times the number of optimization parameters. To ensure a comprehensive exploration of the parameter space, this process was repeated 100 times from independent, uniformly distributed random starting populations, representing a total of 9000 unique starting trajectories. Each run was carried out for a maximum of 18,000 iterations or until a convergence criterion was met, defined as a relative change in the objective function (Equation (14)) of less than 10^{-6} over 20 consecutive iterations.

The 20 best-performing parameter sets from the global search were subsequently refined using MATLAB 2024b's pattern-search algorithm, eventually converging to the two distinct local minima discussed as Case A and Case B. These two final parameter sets effectively reproduced the experimental CV data for Cu and were selected for further analysis.

Subsequently, the identified parameter sets for Cu in Cases A and B were used as the initial parameters for a sequence of local optimizations again using MATLAB 2024b's pattern search algorithm for each CuZn alloy composition in order of increasing Zn content: Cu → CuZn10 → CuZn20 → CuZn25. In each step, the optimized parameter set from the preceding composition served as the initial guess.

CVs from three independent experiments were interpolated to a common time base of 640 equally spaced data points (1 point every 5 mV) using linear interpolation and averaged to obtain mean CVs for model parameterization (Figures S4–S7).

To mitigate the risk of overfitting while capturing processes across different time scales, scan rates of 200 and 50 $\mathrm{mV\ s^{-1}}$ were used for model parameterization (training data). The remaining scan rates (300, 150, 100, and 75 $\mathrm{mV\ s^{-1}}$) were used for model validation.

The objective function f_{obj} for the optimization was the normalized root mean squared error between the simulated and experimentally determined current densities.

1864564x, 2026, 21, Downloaded from https://chemistry-europe.onlinelibrary.wiley.com/doi/10.1002/cssc.70800 by Karlsruher Institut Fur Technologie, Wiley Online Library on [10/11/2026]. See the Terms and Conditions (https://onlinelibrary.wiley.com/terms-and-conditions) on Wiley Online Library for rules of use; OA articles are governed by the applicable Creative Commons License

$$f_{\text{obj}} = \frac{1}{\mathcal{N}} \sum_{\nu=1}^{\mathcal{N}} \frac{\sqrt{\frac{1}{N}\sum_{n=1}^{N}\left(j_{\text{sim},\nu,n} - j_{\text{exp},\nu,n}\right)^2}}{\max(|j_{\text{exp},\nu}|)} \quad (14)$$

where $\mathcal{N}$ is the number of scan rates used for parameter identification, N is the number of data points, and $j_{\text{sim},n}$ and $j_{\text{exp},n}$ are the corresponding simulated and experimental values of the current density at each data point during the third CV cycle.

The normalization of the data by the maximum current density observed during that specific experiment ensured a fair comparison across different scan rates and alloy compositions, where the current density varies significantly. All parameter optimizations were performed using MATLAB 2024b.

6.1.3 | *Density Functional Theory Calculation Details*

DFT calculations with periodic boundary conditions were conducted using the Vienna Ab initio Simulation Package (VASP) version 6.3.0 [74, 75]. The calculations employed the nonlocal BEEF–vdW exchange–correlation functional [76, 77] and projector-augmented wave pseudopotentials [78, 79]. A 4×4 four-layer slab of (111) surface and an energy cutoff of 450 eV were used, in connection with a $3 \times 3 \times 1$ Γ-centered k-point mesh, which we found to be well converged (Figure S12). The applied sawtooth potential, ranging from 0.25 to $-1.00\,\text{V}\,\text{Å}^{-1}$, follows the VASP implementation and generates a homogeneous electric field along the z-axis, within which the surface is relaxed both with and without adsorbates (CO_2 and CO). The corresponding electrode potential E can be related to the field strength E_z (refer to the Supporting Information for details) [48].

The results obtained using the sawtooth approach were then extended by calculating GC adsorption energies with VASPsol. To obtain the GC energies, a constant charge ranging from 0 to $-2.25\,\text{V}\,\text{Å}^{-1}$ ($-3.00\,\text{V}\,\text{Å}^{-1}$ for chemisorbed CO_2) was applied using implicit solvation as implemented in VASPsol [80, 81]. To ensure meaningful values for the electron chemical potential, a symmetric slab was constructed with adsorbate molecules placed on both sides. To relate these results to the experimental scale, we used the computational ferrocenium electrode as the reference electrode [50, 51]. More computational details can be found in the Supporting Information.

Acknowledgments

The authors acknowledge S. Black and M. Ciftdag for their assistance with the CV measurements and Dr. D. I. Sharapa for discussions on computational details. L.S. and F.S. acknowledge support from the state of Baden-Württemberg through bwHPC and the German Research Foundation (DFG) through grant no. INST40/575-1FUGG (JUSTUS2cluster, RVs bw17D011) and the Equal4ETOS project (FKZ 03ZU1205UA) of the BMFTR-funded Zukunftscluster ETOS. The support of the Helmholtz Association is also gratefully acknowledged. G.K. acknowledges the Novo Nordisk Fonden for grant no. 0085735. During the preparation of this manuscript, the authors used Writefull AI to polish the language of the manuscript (accessed February 2026). All AI-generated suggestions were reviewed, revised, and approved by the authors, who take full responsibility for the accuracy and integrity of the work.

Open Access funding enabled and organized by Projekt DEAL.

Funding

This study was supported by the Helmholtz-Gemeinschaft, Novo Nordisk Fonden (0085735) and Bundesministerium für Forschung, Technologie und Raumfahrt (03ZU1205UA).

Conflicts of Interest

The authors declare no conflicts of interest.

Data Availability Statement

The data that support the findings of this study are openly available in the KITopen repository. The experimental measurements and the results of the kinetic modeling can be accessed at https://doi.org/10.35097/shv7ushtuddj8xz6, while the DFT-obtained data are available at https://doi.org/10.35097/55853f8gc1b5xbu8.

References

1. J. Resasco and A. T. Bell, "Electrocatalytic CO_2 Reduction to Fuels: Progress and Opportunities," *Trends in Chemistry* 2 (2020): 825, https://doi.org/10.1016/j.trechm.2020.06.007.

2. B. J. M. Etzold, U. Krewer, S. Thiele, A. Dreizler, E. Klemm, and T. Turek, "Understanding the Activity Transport Nexus in Water and CO_2 Electrolysis: State of the Art, Challenges and Perspectives," *Chemical Engineering Journal* 424 (2021): 130501, https://doi.org/10.1016/j.cej.2021.130501.

3. I. Dorner, P. Röse, and U. Krewer, "Dynamic Vs. Stationary Analysis of Electrochemical Carbon Dioxide Reduction: Profound Differences in Local States," *ChemElectroChem* 10 (2023): e202300387, https://doi.org/10.1002/celc.v10.24.

4. S. Popović, M. Smiljanić, P. Jovanovič, J. Vavra, R. Buonsanti, and N. Hodnik, "Stability and Degradation Mechanisms of Copper-Based Catalysts for Electrochemical CO_2 Reduction," *Angewandte Chemie International Edition* 59 (2020): 14736, https://doi.org/10.1002/anie.v59.35.

5. J. Vavra, T. Shen, D. Stoian, V. Tileli, and R. Buonsanti, "Real-time Monitoring Reveals Dissolution/Redeposition Mechanism in Copper Nanocatalysts during the Initial Stages of the CO_2 Reduction Reaction," *Angewandte Chemie International Edition* 60 (2021): 1347, https://doi.org/10.1002/anie.v60.3.

6. J. A. Rabinowitz and M. W. Kanan, "The Future of Low-Temperature Carbon Dioxide Electrolysis Depends on Solving One Basic Problem," *Nature Communications* 11 (2020): 5231, https://doi.org/10.1038/s41467-020-19135-8.

7. Y. Xie, P. Ou, X. Wang, et al., "High Carbon Utilization in CO_2 Reduction to Multi-Carbon Products in Acidic Media," *Nature Catalysis* 5 (2022): 564, https://doi.org/10.1038/s41929-022-00788-1.

8. G. Marcandalli, M. C. O. Monteiro, A. Goyal, and M. T. M. Koper, "Electrolyte Effects on CO_2 Electrochemical Reduction to CO," *Accounts of Chemical Research* 55 (2022): 1900, https://doi.org/10.1021/acs.accounts.2c00080.

9. N. Govindarajan, A. Xu, and K. Chan, "How pH Affects Electrochemical Processes," *Science* 375 (2022): 379, https://doi.org/10.1126/science.abj2421.

10. I. Dorner, J. Osiewacz, P. Röse, et al., "Control of Electrolyte Intrusion in Carbon-Free Silver Gas Diffusion Electrodes for Electrochemical CO_2 Reduction," *Journal of CO_2 Utilization* 99 (2025): 103163, https://doi.org/10.1016/j.jcou.2025.103163.

11. S. Ringe, E. L. Clark, J. Resasco, et al., "Understanding Cation Effects in Electrochemical CO_2 Reduction," *Energy & Environmental Science* 12 (2019): 3001, https://doi.org/10.1039/C9EE01341E.

12. Y. Xu, Z. Xia, W. Gao, H. Xiao, and B. Xu, "Cation Effect on the Elementary Steps of the Electrochemical CO Reduction Reaction on

1864564x, 2026, 21, Downloaded from https://chemistry-europe.onlinelibrary.wiley.com/doi/10.1002/cssc.70800 by Karlsruher Institut Fur Technologie, Wiley Online Library on [10/11/2026]. See the Terms and Conditions (https://onlinelibrary.wiley.com/terms-and-conditions) on Wiley Online Library for rules of use; OA articles are governed by the applicable Creative Commons License

Cu," *Nature Catalysis* 7 (2024): 1120, https://doi.org/10.1038/s41929-024-01227-z.

13. M. König, J. Vaes, E. Klemm, and D. Pant, "Solvents and Supporting Electrolytes in the Electrocatalytic Reduction of CO_2," *iScience* 19 (2019): 135, https://doi.org/10.1016/j.isci.2019.07.014.

14. C. Deacon-Price, A. H. M. da Silva, C. S. Santana, M. T. M. Koper, and A. C. Garcia, "Solvent Effect on Electrochemical CO_2 Reduction Reaction on Nanostructured Copper Electrodes," *The Journal of Physical Chemistry C* 127 (2023): 14518, https://doi.org/10.1021/acs.jpcc.3c03257.

15. Y. Hori, "Electrochemical CO_2 Reduction on Metal Electrodes," in *Modern Aspects of Electrochemistry*, eds. C. G. Vayenas, R. E. White and M. E. Gamboa-Aldeco (New York, NY: Springer), 2008, pp. 89–189, 42, https://doi.org/10.1007/978-0-387-49489-0_3.

16. E. A. dos Reis, G. T. S. T. da Silva, E. I. Santiago, and C. Ribeiro, "Revisiting Electrocatalytic CO_2 Reduction in Nonaqueous Media: Promoting CO_2 Recycling in Organic Molecules by Controlling H_2 Evolution," *Energy Technology* 11 (2023): 2201367, https://doi.org/10.1002/ente.v11.6.

17. H. Liu, M. Yu, X. Tong, Q. Wang, and M. Chen, "High Temperature Solid Oxide Electrolysis for Green Hydrogen Production," *Chemical Reviews* 124 (2024): 10509, https://doi.org/10.1021/acs.chemrev.3c00795.

18. Y. A. Daza and J. N. Kuhn, "CO_2 Conversion by Reverse Water Gas Shift Catalysis: Comparison of Catalysts, Mechanisms and Their Consequences for CO_2 Conversion to Liquid Fuels," *RSC Advances* 6 (2016): 49675, https://doi.org/10.1039/C6RA05414E.

19. S. Neyrizi, M. A. Hempenius, and G. Mul, "Performance of Transition Metals in Imidazolium-Assisted CO_2 Reduction in Acetonitrile," *ChemElectroChem* 11 (2024): e202300383, https://doi.org/10.1002/celc.v11.11.

20. M. König, S.-H. Lin, J. Vaes, D. Pant, and E. Klemm, "Integration of Aprotic CO_2 Reduction to Oxalate at a Pb Catalyst into a GDE Flow Cell Configuration," *Faraday Discussions* 230 (2021): 360, https://doi.org/10.1039/D0FD00141D.

21. M. König, J. Vaes, D. Pant, and E. Klemm, "Effect of Solvents on Aprotic CO_2 Reduction: A Study on the Role of CO_2 Mass Transport in the Product Selectivity between Oxalate and Carbon Monoxide," *The Journal of Physical Chemistry C* 127 (2023): 18159, https://doi.org/10.1021/acs.jpcc.3c03992.

22. T. Mairegger, H. Li, C. Grießer, et al., "Electroreduction of CO_2 in a Non-Aqueous Electrolyte—the Generic Role of Acetonitrile," *ACS Catalysis* 13 (2023): 5780, https://doi.org/10.1021/acscatal.3c00236.

23. W. Chen, X. Du, S. Tao, et al., "Electrolyte Effects on Reaction Kinetics in Electrochemical CO_2 Reduction: The Roles of pH, Cations, and Anions," *Chemical Physics Reviews* 6 (2025): 011302, https://doi.org/10.1063/5.0242304.

24. F. Longhin, M. Rodrigues Pinto, Q. Xu, and B. Seger, "CO Adsorption Dynamics during CO_2 Electrolysis in Aprotic Organic Electrolytes," *ACS Applied Materials & Interfaces* 17 (2025): 36596, https://doi.org/10.1021/acsami.5c03519.

25. J.-M. McGregor, J. T. Bender, A. S. Petersen, et al., "Organic Electrolyte Cations Promote Non-Aqueous CO_2 Reduction by Mediating Interfacial Electric Fields," *Nature Catalysis* 8 (2025): 79, https://doi.org/10.1038/s41929-024-01278-2.

26. H. A. Hansen, C. Shi, A. C. Lausche, A. A. Peterson, and J. K. Nørskov, "Bifunctional Alloys for the Electroreduction of CO_2 and CO," *Physical Chemistry Chemical Physics* 18 (2016): 9194, https://doi.org/10.1039/C5CP07717F.

27. O. Zoubir, L. Atourki, H. A. Ahsaine, and A. BaQais, "Current State of Copper-Based Bimetallic Materials for Electrochemical CO_2 Reduction: A Review," *RSC Advances* 12 (2022): 30056, https://doi.org/10.1039/D2RA05385C.

28. H. S. Jeon, J. Timoshenko, F. Scholten, et al., "Operando Insight into the Correlation between the Structure and Composition of CuZn Nanoparticles and Their Selectivity for the Electrochemical CO_2 Reduction," *Journal of the American Chemical Society* 141 (2019): 19879, https://doi.org/10.1021/jacs.9b10709.

29. M. L. J. Peerlings, K. Han, A. Longo, et al., "Synthesis and Catalytic Performance of Bimetallic Oxide-Derived CuO–ZnO Electrocatalysts for CO_2 Reduction," *ACS Catalysis*. (2024): 10701–10711, https://doi.org/10.1021/acscatal.4c01575.

30. T.-U. Wi, Z. H. Levell, S. Hao, et al., "Selective and Stable Ethanol Synthesis via Electrochemical CO_2 Reduction in a Solid Electrolyte Reactor," *ACS Energy Letters* 10 (2025): 822, https://doi.org/10.1021/acsenergylett.4c03091.

31. M. Behrens, F. Studt, I. Kasatkin, et al., "The Active Site of Methanol Synthesis over $Cu/ZnO/Al_2O_3$ Industrial Catalysts," *Science* 336 (2012): 893, https://doi.org/10.1126/science.1219831.

32. F. Studt, M. Behrens, E. L. Kunkes, et al., "The Mechanism of CO and CO_2 Hydrogenation to Methanol over Cu-Based Catalysts," *ChemCatChem* 7 (2015): 1105, https://doi.org/10.1002/cctc.v7.7.

33. K. P. Kuhl, T. Hatsukade, E. R. Cave, D. N. Abram, J. Kibsgaard, and T. F. Jaramillo, "Electrocatalytic Conversion of Carbon Dioxide to Methane and Methanol on Transition Metal Surfaces," *Journal of the American Chemical Society* 136 (2014): 14107, https://doi.org/10.1021/ja505791r.

34. J. Zhang, C. Guo, S. Fang, et al., "Accelerating Electrochemical CO_2 Reduction to Multi-Carbon Products via Asymmetric Intermediate Binding at Confined Nanointerfaces," *Nature Communications* 14 (2023): 1298, https://doi.org/10.1038/s41467-023-36926-x.

35. Y. Feng, Z. Li, H. Liu, et al., "Laser-Prepared CuZn Alloy Catalyst for Selective Electrochemical Reduction of CO_2 to Ethylene," *Langmuir* 34 (2018): 13544, https://doi.org/10.1021/acs.langmuir.8b02837.

36. G. Pacchioni, "From CO_2 to Methanol on $Cu/ZnO/Al_2O_3$ Industrial Catalyst. What Do We Know About the Active Phase and the Reaction Mechanism?," *ACS Catalysis* 14 (2024): 2730, https://doi.org/10.1021/acscatal.3c05669.

37. R. Witzel, L. Wildersinn, E. Tusini, et al., "Investigation of the Performance and Stability of Copper and Brass Nanoparticles for CO_2 Reduction in Organic Electrolytes," *Journal of CO_2 Utilization* 97 (2025): 103138, https://doi.org/10.1016/j.jcou.2025.103138.

38. N. Oppel, P. Röse, S. Heuser, M. Prokein, U.-P. Apfel, and U. Krewer, "Unveiling the Kinetics of CO_2 Reduction in Aprotic Electrolyte: The Critical Role of Adsorption," *Electrochimica Acta* 490 (2024): 144270, https://doi.org/10.1016/j.electacta.2024.144270.

39. J. Geppert, F. Kubannek, P. Röse, and U. Krewer, "Identifying the Oxygen Evolution Mechanism by Microkinetic Modelling of Cyclic Voltammograms," *Electrochimica Acta* 380 (2021): 137902, https://doi.org/10.1016/j.electacta.2021.137902.

40. J. Geppert, P. Röse, S. Czioska, et al., "Microkinetic Analysis of the Oxygen Evolution Performance at Different Stages of Iridium Oxide Degradation," *Journal of the American Chemical Society* 144 (2022): 13205, https://doi.org/10.1021/jacs.2c03561.

41. J. Geppert, P. Röse, S. Pauer, and U. Krewer, "Microkinetic Barriers of the Oxygen Evolution on the Oxides of Iridium, Ruthenium and Their Binary Mixtures," *ChemElectroChem* 9 (2022): e202200481, https://doi.org/10.1002/celc.v9.20.

42. F. Dattila, R. R. Seemakurthi, Y. Zhou, and N. López, "Modeling Operando Electrochemical CO_2 Reduction," *Chemical Reviews* 122 (2022): 11085, https://doi.org/10.1021/acs.chemrev.1c00690.

43. C. Zhan, F. Dattila, C. Rettenmaier, et al., "Key Intermediates and Cu Active Sites for CO_2 Electroreduction to Ethylene and Ethanol," *Nature Energy* 9 (2024): 1485, https://doi.org/10.1038/s41560-024-01633-4.

1864564x, 2026, 21, Downloaded from https://chemistry-europe.onlinelibrary.wiley.com/doi/10.1002/cssc.70800 by Karlsruher Institut Fur Technologie, Wiley Online Library on [10/11/2026]. See the Terms and Conditions (https://onlinelibrary.wiley.com/terms-and-conditions) on Wiley Online Library for rules of use; OA articles are governed by the applicable Creative Commons License

44. J. K. Nørskov, J. Rossmeisl, A. Logadottir, et al., "Origin of the Overpotential for Oxygen Reduction at a Fuel-Cell Cathode," *The Journal of Physical Chemistry B* 108 (2004): 17886, https://doi.org/10.1021/jp047349j.

45. H. Oberhofer, "Electrocatalysis Beyond the Computational Hydrogen Electrode," in *Handbook of Materials Modeling: Applications: Current and Emerging Materials*, eds. W. Andreoni and S. Yip (Cham: Springer International Publishing, 2018), pp. 1–33, https://doi.org/10.1007/978-3-319-50257-1_9-1.

46. A. Bagger, O. Christensen, V. Ivaništšev, and J. Rossmeisl, "Catalytic CO_2/CO Reduction: Gas, Aqueous, and Aprotic Phases," *ACS Catalysis* 12 (2022): 2561, https://doi.org/10.1021/acscatal.1c05358.

47. R. J. Gomes, C. Birch, M. M. Cencer, et al., "Probing Electrolyte Influence on CO_2 Reduction in Aprotic Solvents," *The Journal of Physical Chemistry C* 126 (2022): 13595, https://doi.org/10.1021/acs.jpcc.2c03321.

48. A. M. Dudzinski, E. Diesen, K. Reuter, and V. J. Bukas, "Oxygen Adsorption at the Electrochemical Metal/Water Interface: Au(111) Vs Pt(111)," *The Journal of Physical Chemistry C* 128 (2024): 20886, https://doi.org/10.1021/acs.jpcc.4c06384.

49. K. Schwarz and R. Sundararaman, "The Electrochemical Interface in First-Principles Calculations," *Surface Science Reports* 75 (2020): 100492, https://doi.org/10.1016/j.surfrep.2020.100492.

50. A. S. Kramarenko, D. I. Sharapa, E. A. Pidko, and F. Studt, "Ab Initio Kinetics of Electrochemical Reactions Using the Computational Fc^0/Fc^+ Electrode," *The Journal of Physical Chemistry A* 128 (2024): 9063, https://doi.org/10.1021/acs.jpca.4c04923.

51. L. Savintseva, P. Neugebauer, D. I. Sharapa, P. Röse, U. Krewer, and F. Studt, "The Electrochemical Shono Oxidation of *N*-Formylpyrrolidine: Mechanistic Insights from the Computational Ferrocene Electrode Model and Cyclic Voltammetry," *ChemElectroChem* 12 (2025): e202500202, https://doi.org/10.1002/celc.v12.19.

52. O. van der Heijden, S. Park, R. E. Vos, J. J. J. Eggebeen, and M. T. M. Koper, "Tafel Slope Plot as a Tool to Analyze Electrocatalytic Reactions," *ACS Energy Letters* 9 (2024): 1871, https://doi.org/10.1021/acsenergylett.4c00266.

53. A. M. Limaye, J. S. Zeng, A. P. Willard, and K. Manthiram, "Bayesian Data Analysis Reveals No Preference for Cardinal Tafel Slopes in CO_2 Reduction Electrocatalysis," *Nature Communications* 12 (2021): 703, https://doi.org/10.1038/s41467-021-20924-y.

54. A. Gennaro, A. A. Isse, and E. Vianello, "Solubility and Electrochemical Determination of CO_2 in Some Dipolar Aprotic Solvents," *Journal of Electroanalytical Chemistry and Interfacial Electrochemistry* 289 (1990): 203, https://doi.org/10.1016/0022-0728(90)87217-8.

55. M. T. Tyn and W. F. Calus, "Diffusion Coefficients in Dilute Binary Liquid Mixtures," *Journal of Chemical and Engineering Data* 20 (1975): 106, https://doi.org/10.1021/je60064a006.

56. N. N. Lam, P. D. Docherty, and R. Murray, "Practical Identifiability of Parametrised Models: A Review of Benefits and Limitations of Various Approaches," *Mathematics and Computers in Simulation* 199 (2022): 202, https://doi.org/10.1016/j.matcom.2022.03.020.

57. M. Schulze, S. Triemer, R. Schenkendorf, A. Seidel-Morgenstern, and U. Krewer, "Identifying a Kinetic Model for the Acid-Catalyzed Sequence of the Artemisinin Partial Synthesis," *Chemical Engineering Journal* 523 (2025): 167770, https://doi.org/10.1016/j.cej.2025.167770.

58. L. Wang, H. Peng, S. Lamaison, et al., "Bimetallic Effects on Zn-Cu Electrocatalysts Enhance Activity and Selectivity for the Conversion of CO_2 to CO," *Chem Catalysis* 1 (2021): 663, https://doi.org/10.1016/j.checat.2021.05.006.

59. M. C. Figueiredo, I. Ledezma-Yanez, and M. T. M. Koper, "In Situ Spectroscopic Study of CO_2 Electroreduction at Copper Electrodes in Acetonitrile," *ACS Catalysis* 6 (2016): 2382, https://doi.org/10.1021/acscatal.5b02543.

60. A. Wuttig, C. Liu, Q. Peng, et al., "Tracking a Common Surface-Bound Intermediate during CO_2-to-Fuels Catalysis," *ACS Central Science* 2 (2016): 522, https://doi.org/10.1021/acscentsci.6b00155.

61. A. T. Chu and Y. Surendranath, "Aprotic Solvent Exposes an Altered Mechanism for Copper-Catalyzed Ethylene Electrosynthesis," *Journal of the American Chemical Society* 144 (2022): 5359, https://doi.org/10.1021/jacs.1c12595.

62. B. Tian, Y. Xu, H. Wu, et al., "Acetonitrile-Driven Universal CO Production across Diverse Metal Catalysts," *Science China Chemistry*. 68 (2024): 2110–2116, https://doi.org/10.1007/s11426-024-2416-0.

63. M. Xu, Ab Initio Dynamics in Catalysis, Ph.D. thesis, Department of Physics, Technical University of Denmark, 2024,

64. S. Ringe, "The Importance of a Charge Transfer Descriptor for Screening Potential CO_2 Reduction Electrocatalysts," *Nature Communications* 14 (2023): 2598, https://doi.org/10.1038/s41467-023-37929-4.

65. J. H. Lee, S. Kattel, Z. Jiang, et al., "Tuning the Activity and Selectivity of Electroreduction of CO_2 to Synthesis Gas Using Bimetallic Catalysts," *Nature Communications* 10 (2019): 3724, https://doi.org/10.1038/s41467-019-11352-0.

66. D. Cheng, K.-L. C. Nguyen, V. Sumaria, et al., "Structure Sensitivity and Catalyst Restructuring for CO_2 Electro-reduction on Copper," *Nature Communications* 16 (2025): 4064, https://doi.org/10.1038/s41467-025-59267-3.

67. B. Tran and B. R. Goldsmith, "Theoretical Investigation of the Potential-Dependent CO Adsorption on Copper Electrodes," *The Journal of Physical Chemistry Letters* 15 (2024): 6538–6543, https://doi.org/10.1021/acs.jpclett.4c01032.

68. C. Amatore and J. M. Savéant, "Mechanism and Kinetic Characteristics of the Electrochemical Reduction of Carbon Dioxide in Media of Low Proton Availability," *Journal of the American Chemical Society* 103 (1981): 5021, https://doi.org/10.1021/ja00407a008.

69. S. Ikeda, T. Takagi, and K. Ito, "Selective Formation of Formic Acid, Oxalic Acid, and Carbon Monoxide by Electrochemical Reduction of Carbon Dioxide," *Bulletin of the Chemical Society of Japan* 60 (1987): 2517, https://doi.org/10.1246/bcsj.60.2517.

70. T. Vidaković, M. Christov, and K. Sundmacher, "Rate Expression for Electrochemical Oxidation of Methanol on a Direct Methanol Fuel Cell Anode," *Journal of Electroanalytical Chemistry* 580 (2005): 105, https://doi.org/10.1016/j.jelechem.2005.03.015.

71. U. Krewer, M. Christov, T. Vidakovic', and K. Sundmacher, "Impedance Spectroscopic Analysis of the Electrochemical Methanol Oxidation Kinetics," *Journal of Electroanalytical Chemistry* 589 (2006): 148, https://doi.org/10.1016/j.jelechem.2006.01.027.

72. E. J. F. Dickinson, J. G. Limon-Petersen, N. V. Rees, and R. G. Compton, "How Much Supporting Electrolyte Is Required to Make a Cyclic Voltammetry Experiment Quantitatively "Diffusional"? a Theoretical and Experimental Investigation," *The Journal of Physical Chemistry C* 113 (2009): 11157, https://doi.org/10.1021/jp901628h.

73. A. J. Bard, L. R. Faulkner, and H. S. White, *Electrochemical Methods: Fundamentals and Applications* (Hoboken, NJ: Wiley, 2022).

74. G. Kresse and J. Furthmüller, "Efficiency of Ab-Initio Total Energy Calculations for Metals and Semiconductors Using a Plane-Wave Basis Set," *Computational Materials Science* 6 (1996): 15, https://doi.org/10.1016/0927-0256(96)00008-0.

75. G. Kresse and J. Furthmüller, "Efficient Iterative Schemes for *Ab Initio* Total-Energy Calculations Using a Plane-Wave Basis Set," *Physical Review B* 54 (1996): 11169, https://doi.org/10.1103/PhysRevB.54.11169.

76. J. J. Mortensen, K. Kaasbjerg, S. L. Frederiksen, J. K. Nørskov, J. P. Sethna, and K. W. Jacobsen, "Bayesian Error Estimation in

1864564x, 2026, 21, Downloaded from https://chemistry-europe.onlinelibrary.wiley.com/doi/10.1002/cssc.70800 by Karlsruher Institut Fur Technologie, Wiley Online Library on [10/11/2026]. See the Terms and Conditions (https://onlinelibrary.wiley.com/terms-and-conditions) on Wiley Online Library for rules of use; OA articles are governed by the applicable Creative Commons License

Density-Functional Theory," *Physical Review Letters* 95 (2005): 216401, https://doi.org/10.1103/PhysRevLett.95.216401.

77. J. Wellendorff, K. T. Lundgaard, A. Møgelhøj, et al., "Density Functionals for Surface Science: Exchange-Correlation Model Development with Bayesian Error Estimation," *Physical Review B* 85 (2012): 235149, https://doi.org/10.1103/PhysRevB.85.235149.

78. P. E. Blöchl, "Projector Augmented-Wave Method," *Physical Review B* 50 (1994): 17953, https://doi.org/10.1103/PhysRevB.50.17953.

79. G. Kresse and D. Joubert, "From Ultrasoft Pseudopotentials to the Projector Augmented-Wave Method," *Physical Review B* 59 (1999): 1758, https://doi.org/10.1103/PhysRevB.59.1758.

80. K. Mathew, R. Sundararaman, K. Letchworth-Weaver, T. A. Arias, and R. G. Hennig, "Implicit Solvation Model for Density-Functional Study of Nanocrystal Surfaces and Reaction Pathways," *The Journal of Chemical Physics* 140 (2014): 084106, https://doi.org/10.1063/1.4865107.

81. K. Mathew, V. S. C. Kolluru, S. Mula, S. N. Steinmann, and R. G. Hennig, "Implicit Self-Consistent Electrolyte Model in Plane-Wave Density-Functional Theory," *The Journal of Chemical Physics* 151 (2019): 234101, https://doi.org/10.1063/1.5132354.

Supporting Information

Additional supporting information can be found online in the Supporting Information section.

1864564x, 2026, 21, Downloaded from https://chemistry-europe.onlinelibrary.wiley.com/doi/10.1002/cssc.70800 by Karlsruher Institut Fur Technologie, Wiley Online Library on [10/11/2026]. See the Terms and Conditions (https://onlinelibrary.wiley.com/terms-and-conditions) on Wiley Online Library for rules of use; OA articles are governed by the applicable Creative Commons License